Modelling and Numerical Investigation of Taylor Flow on the Performance of Electrochemical Flow Cells

Chaitanya Bhatraju

Faculty of Applied sciences

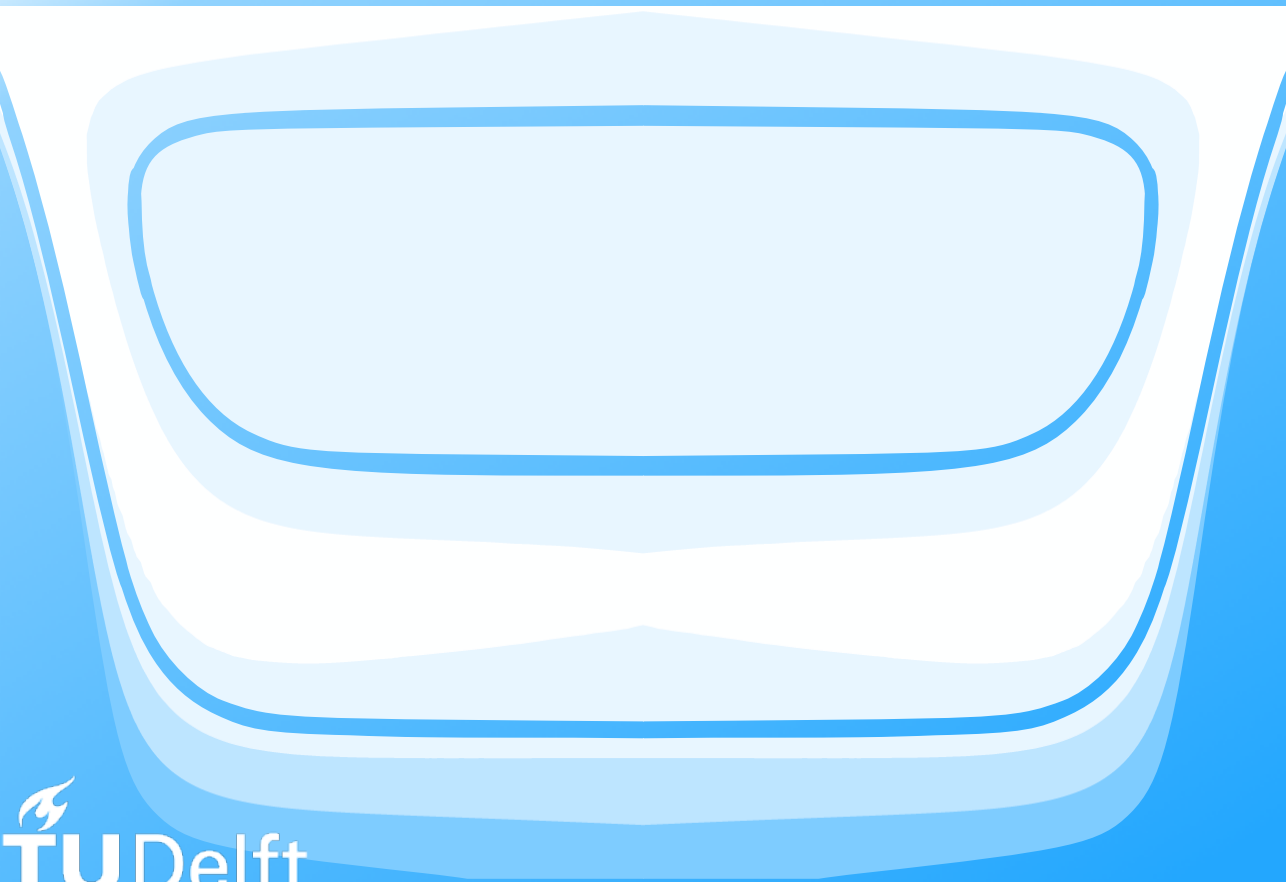

TU Delft

Modelling and Numerical Investigation of Taylor Flow on the Performance of Electrochemical Flow Cells

by

Chaitanya Bhatraju

to obtain the degree of
Master of Science in Chemical engineering,
at the Delft University of Technology,
to be defended publicly on Thursday May 14, 2020 at 14:30.

Thesis supervisors:	Prof. dr. ir. J.R. van Ommen
	Dr. ir. V. van Steijn
PhD supervisor:	I. Bagemihl
Thesis committee:	Prof. dr. ir. J.R. van Ommen
	Dr. ir. V. van Steijn
	Dr. ir. D. A. Vermaas

TU Delft Delft University of Technology

e-Refinery
Towards sustainable production of chemicals and fuels

Cogito, Ergo Sum
I think, therefore I am

René Descartes

Abstract

Electrochemical reduction of CO_2 using renewable energy sources is one of the promising avenues to pursue towards mitigating the emissions of the notorious CO_2. However, the CO_2 electrolysis in aqueous systems, due to the low solubility of CO_2, are severely limited by mass-transfer. State of the art review shows that a significant amount of the research is done to improve mass-transfer, where a variety of electrolyser designs were studied. Despite the effort, the challenge to enhance mass transfer remains and is the focus of the present work. To improve mass transfer, an innovative concept is proposed - Taylor flow in an electrochemical flow cell.

Taylor flow has been extensively studied in the literature, especially in microchannels and monolith reactors. Therefore the characteristics of the Taylor flow are known to a certain extent. But they were never tested in an electrochemical system. For that reason, a numerical investigation is carried out to assess the performance of Taylor flow on the flow cell. A simplified 2D model was formulated using a unit-cell strategy and is verified based on experimental data and theoretical concepts. The effect of dissolving bubbles is also modelled using a quasi-steady-state analysis

The results of the 2D model show a significant improvement in the performance, i.e. in the current densities of the electrochemical cell compared to a typical flow cell. The maximum calculated current densities increase by an order of magnitude under certain flow conditions. The dissolution studies showed that the current densities deteriorate with time. Nevertheless, the overall performance is still higher than the typical flow cell. Finally, based on the insights from the 2D model, a 1D model is suggested to estimate the current densities and dissolution rates. The present study showed promising results for using Taylor flow in an electrochemical cell. The proposed 2D model can help in aiding future modelling studies while the 1D model can give simple estimates for the experimental work.

Acknowledgements

I wish to express my sincere appreciation to my supervisors Volkert van Steijn and Ruud van Ommen. Volkert has the substance of a genius: he is an all-time inspiration. He took it upon himself to push me to think out of the box. Ruud van Ommen lead all the e-refinery meetings, which helped me to make a better path throughout my Thesis. Without their persistent help, the goal of this project would not have been realized. Heartfelt thanks to my PhD supervisor and the pillar of support, Isabell, who devoted substantial time to have in-depth discussions with me. Her scrutiny and her patience encouraged me to move forward when faced with a road-block.

It's a pleasure to have DA Vermaas on my thesis committee. I am glad that you gracefully accepted my request. I want to pay special regards to Luis Portela for explaining certain aspects of fluid dynamics that helped me with the nuances of my project.

I want to recognize the invaluable assistance that Manu (PhD, TP) provided. I owe my understanding of simulations to him. I am also grateful for the many deliberations with Sayujya Shah, a fellow Masters student at TU Delft, who contributed to my knowledge of the practical aspects of the project.

Not least of all, I wish to thank my family whose emotional assistance was a milestone in the completion of this project, and all my friends, who helped me stay sane.

Chaitanya Bhatraju
Delft, May 2020

Contents

List of Figures

List of Tables

Nomenclature

Abbreviations

AEM	Anion Exchange Membrane
CCS	Carbon Capture Storage
CD	Current Density
CFD	Computational Fluid Dynamics
EE	Energy Efficiency
FD	Faradic Efficiency
FEM	Finite Element Method
GDE	Gas Diffusion Electrodes
HER	Hydrogen Evolution Reaction
IPCC	International Panel on Climate Change
OER	Oxygen Evolution Reaction
RAM	Random Access Memory
SHE	Standard Hydrogen Electrode

Dimensionless constants

Reynolds Number (Re)	$\frac{\rho u_{TP} D}{\mu}$
Capillary Number (Ca_B)	$\frac{\mu u_B}{\sigma}$
Damkohler Number (Da)	$\frac{k(\eta)\delta}{D}$
Peclet Number (Pe)	$\frac{ud}{D}$
Number of electrons transferred	n
Energetic Efficiency	ϵ_{EE}
Faradic Efficiency	ϵ_{FE}
Void Fraction	ϵ_B

List of Symbols

j	Current Density	[A/m^2]
I	Current	[A]
A	Area	[m^2]
E^O	Standard Thermodynamic potential	[V]
F	Faraday's constant	[C/mol]
η	Overpotential	[V]
j_{llm}	Limiting current density	[A/m^2]
v_m	mass transfer rate	[mol/s]
δ	Diffusion layer thickness	[m]
δ_T	Thickness of the liquid film	[m]
δ_N	Nernst Diffusion layer thickness	[m]
δ_{av}	Average Diffusion layer thickness	[m]
d	Diameter of the channel	[m]
μ	Dynamic Viscosity of the liquid	[Pa s]
σ	Surface tension	[N/m]
ρ	Density of liquid	[Kg/m^3]
L_B	Length of Bubble	[m]
L_s	Length of slug	[m]
L_{uc}	Unit Cell Length	[m]
u_B	Bubble velocity	[m/s]
u_{GS}	Superficial gas velocities	[m/s]
u_{LS}	Superficial Liquid velocities	[m/s]
u_{TP}	Two phase velocity	[m/s]
J_i	Molar flux of species "i"	[mol/m^2/s]
C_i	Concentration of species "i"	[mol/m^3]
D_i	Binary Diffusion coefficient of species"i"	[m^2/s]
P	Pressure	[Pa]
C_i^O	Saturated Concentration of species i	[mol/m^3]
H_i	Henry's constant of constant of species 'i'	[atm]
P_B	Pressure inside the bubble	[Pa]
$R_{i,s}$	Surface Reaction rate	[mol/m^2/s]
E_{eq}	Equillibrium potential	[V]
$E^{o'}$	Formal potentials	[V]
$C_{i,s}$	Surface concentrations	[mol/m^3]
j_o	Exchange current density	[A/m^2]
E_A	Applied Electrode potential	[V]
$C_{i,b}$	Bulk Concentrations	[mol/m^3]
k	Surface reaction constant	[m^2/s]
C_B	Concentration of carbon dioxide inside the bubble	[mol/m^3]
V_B	Voulme of the Bubble	[m^3]
J_{I,CO_2}	Flux at Interface	[mol/m^2/s]
k_L	Mass transfer coefficient at Interface	[mol/s]
C_i^{Ref}	Reference concentration	[mol/m^3]
R_v	Vortex centre	[m]
a	Specific surface area	[1/m]
$\bar{C}$	Average Concentration	[mol/m^3]
α_c	Transfer coefficient of cathode	-
ν_i	stochiometry coefficient	-

1

Introduction

Electrochemical reduction of Carbon dioxide (CO_2) into value-added products is an attractive solution to reduce CO_2 emissions and mitigate global warming. In this thesis, the author assesses the performance, numerically, of electrochemical reduction of CO_2 to Carbon monoxide (CO) in the presence of Taylor flow.

Human lifestyle, starting from eating food at home to travelling around the world, has created a high energy demand. Energy demand, at present, is being met by burning fossil fuels releasing, in the process, a large amount of CO_2 into the atmosphere. Increase in CO_2 concentrations, along with other greenhouse gases, in the atmosphere, lead to the current scenario of climate change and global warming. To mitigate the effects of global warming, Intergovernmental Panel on Climate Change (IPCC) studied and showed that CO_2 emissions should decrease by 2050 to 50-80% of the emission levels of the year 2000[1, 2].

Carbon Capture and Storage (CCS) at production facilities such as steel industries and power plants, to name a few, is a well-known approach to reduce emissions in the atmosphere. CCS can only be a *temporary* or a secondary solution, as the net emission after implementing this solution is still positive[3]. The process itself is energy-intensive and it is a challenge to implement in industries such as the transportation sector, which attribute to 25% of carbon emissions[4]. It also does not address the issue of using already-depleting, non-renewable fossil fuels. Using renewable energy sources as an alternative to fossil fuels is a lucrative solution. A lot of scientific communities are researching it as they are present abundantly and are sustainable energy sources. At present, technologies based on renewable energy are used to generate sustainable electricity. These processes often suffer from the intermittent nature of the energy supply. One long-term solution is to use CO_2 from CCS and electricity from renewable resources to produce useful chemicals and fuels. This way, renewable energy can be stored in the form of chemical bonds while consuming deserted CO_2.

1

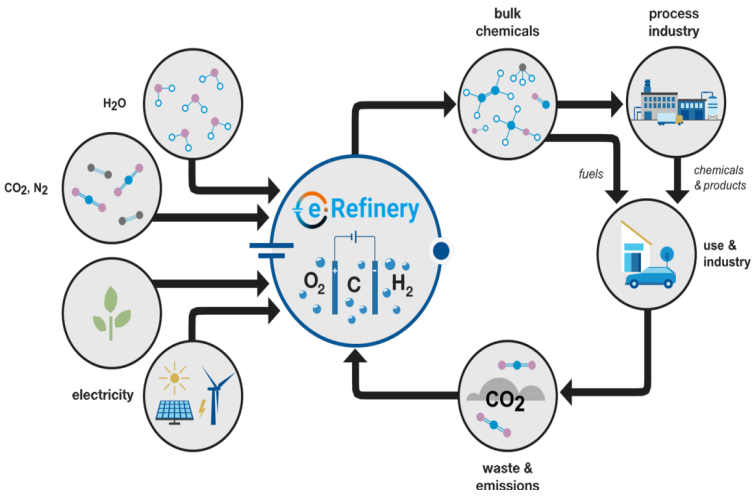

Figure 1.1: The e-Refinery concept[5]

Utilising CO_2 to produce useful products through chemical or electrochemical conversion has the potential to be an immediate[6], long-term, sustainable solution. Kauffman et al. [7] using simple estimates showed that electricity produced from renewable sources is enough to power large-scale CO_2 conversion systems highlighting the potential of *electrochemical reduction of CO_2* in mitigating global warming. e-Refinery initiative at TU Delft is helping in accelerating the shift from the fossil-based chemical industry to a sustainable electricity-based system. It tries to solve these challenges by using sustainable electricity from renewables to produce fuels and chemical building blocks by building on the fundamentals of electrochemistry[5]. As shown in Figure 1.1, the artificial carbon cycle or artificial photosynthesis is one of the key solutions among many that e-Refinery aims to achieve. In this thesis, the focus is on the utilisation of CO_2 through electrochemical reduction to produce useful chemicals.

1.1. CO_2 Electrolysis to CO

Depending on the number of electrons transferred, electrochemical reduction of CO_2 produces various types of products. C_1 products such as Carbon monoxide, Formic acid, C_2 products such as Ethylene, Ethanol, C_3 products such as n-Propanol, were directly produced using state-of-the-art catalysts. Techno-economic analyses done by Bushuyev et al. [6], Verma et al. [8], Kibria et al. [9] found that the short-chain products such as CO, Formate are economically attractive. The analyses were based on the market size, market price, capital costs and operational costs for each product. Although, the market size for CO and Formic acid is relatively small[9] compared to longer chain molecules such as Ethylene and Proponal; the operational costs for long-chain products were much higher due to low selectivi-

ties and increased energy requirements[6]. Carbon monoxide, CO, is particularly compelling because the products form Syngas (CO+H_2) which can be used as a building block to produce hydrocarbon fuels using the Fischer Tropsch process or generate electricity[10]. Syngas production also eliminates the need for separation of products after electrolysis. Kim et al. [11] suggested that *"the electrochemical conversion of CO_2 to CO can be performed efficiently while using a diluted CO_2 stream, such as flue gas"* reducing the cost of CO_2 feed-stock. Thus, production of CO from CO_2 has numerous economic opportunities making it an interesting route to pursue.

In the next section, the author discusses the summary of work that has been done for the production of CO from CO_2 electrolysis and highlights the remaining challenges and opportunities in this field.

1.1.1. Literature Review

In an electrochemical cell, the reactants are converted into products by transfer of electrons at anode and cathode which are represented using half-cell reactions. Half-cell reaction for CO_2 at cathode, for pH = 7, is given by Equation 1.1 and the competing Hydrogen Evolution Reaction(HER) is given by Equation 1.2, where E^o is the standard thermodynamic potential Vs Standard Hydrogen Electrode (SHE). An external power supply provides electrons and the current in the circuit is related to the number of electrons transferred at the electrode per unit time.

$$\mathrm{CO_2 + 2\,e^- + 2\,H^+ \longrightarrow CO + H_2O} \quad E^o = -0.53V \quad vs \quad SHE \tag{1.1}$$

$$\mathrm{2\,H^+ + 2\,e^- \longrightarrow H_2} \quad E^o = 0V \quad vs \quad SHE \tag{1.2}$$

The performance of an electrochemical cell, analogous to a reactor system, is assessed based on conversion, selectivity and efficiency of the process. These are determined by Current Density (CD), Faradic Efficiency (FE) and Energetic Efficiency (EE), respectively. Current density ($j = \frac{I}{A}$) is calculated as current per unit area of the electrode. Faradic Efficiency ($\epsilon_{FE} = \frac{z.n.F}{\int_0^t i.dt}$) is the ratio of the number of electrons transferred to the desired product ($z.n.F$) to the total number of electrons supplied. Equation 1.3 calculates energetic efficiency which gives the part of energy utilised for the production of desired products.

$$\epsilon_{EE} = \frac{E^o \epsilon_{FE}}{E^o + \eta} \tag{1.3}$$

where η is overpotential required for a certain current density. For the commercial realisation of CO_2 electrolysers Kibria et al. [9], based on Techno-Economic Analysis, suggested the following metrics should be met: Current densities greater than 300 $\frac{mA}{cm^2}$[1]; Faradic Efficiency greater than 90%; and Energetic Efficiency between 56 - 70%. From Equation 1.3, it can be seen for a given current density, to

[1]Values are based on commercially operating water electrolyser

1

achieve high energy efficiencies, one would need high Faradic efficiency and low overpotentials. Overpotential can be divided into three types: Activation overpotential, which depends on electrode kinetics; Concentration overpotential, which arises due to mass transfer limitations; and Ohmic overpotential, which arise due to solution resistance. Kinetics, solution resistance and mass transfer depend on the type of catalyst, nature of electrolyte and electrolyser design.

Electrolysers use electrolytes and membranes to facilitate ion transport and reduce solution resistance. Alternatively, using electrolytes and membranes also changes the reaction environment at the electrode surface and is known to affect reaction rates negatively[8, 12]. Operating at low pH, in acidic medium, increases the competition between CO_2 reduction and Hydrogen evolution reaction leading to low Faradic efficiencies of CO. It also adds thermodynamic overpotential on the anode side as the Oxygen Evolution Reaction (OER), which favours basic medium, is occurring in an acidic medium. Similarly, operating at high pH, in basic medium, causes CO_2 dissociation decreasing its availability. Therefore, several strategies are employed in literature to optimise the reaction environment. For excellent state of the art review on reaction environment, the reader is referred to review papers by Kibria et al. [9], Hernández et al. [10], Whipple et al. [13]. For the case of CO production, use of KOH as an electrolyte and Anion Exchange Membrane (AEM) yield best performance results[10, 14, 15].

Silver (Ag) and Gold (Au) are commonly used as a catalyst for CO production, as they achieve high ($> 90\%$) Faradic efficiencies towards CO[10, 16, 17]. One of the main drawbacks of using such catalysts is that they have high activation overpotentials. Nano-structuring catalyst surface showed promising results in reducing the activation overpotentials due to an increase in the intrinsic catalyst activity [9, 11, 18, 19]. Although considerable progress has been made in the field of electro-catalysts, electrolytes and membranes, current densities reported were small, between $5 - 50 \frac{mA}{cm^2}$[14], despite having very high reaction rates and efficiency. The reason was that most of the experiments involving catalysts were designed to determine and characterise the reaction kinetics, and were purposefully done in an H-cell where mass transfer limitations are prominent. Figure 1.2 shows the traditional H-cell, with a membrane separating the catholyte and anolyte, used for the kinetic study.

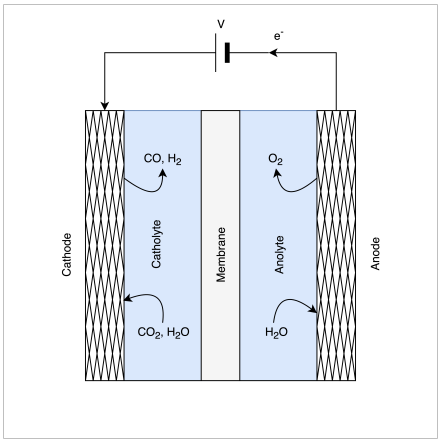

Figure 1.2: H-cell design for CO_2 Electrolysis

Mass transport limitations in CO_2 electrolysis arise due to 2 main reasons: Low

solubility of CO_2 in aqueous electrolyte and low diffusion rates in liquids. Flow cells are introduced to improve mass transfer and to have a continuous supply of CO_2. Two types of flow cells are most commonly used in literature: Liquid-phase electrolyser and the Gas-phase electrolyser. Both of them use Gas Diffusion Electrodes(GDEs) so that reactant, CO_2, is sent directly to the catalyst in the gas phase, thus increasing the mass transfer rate.

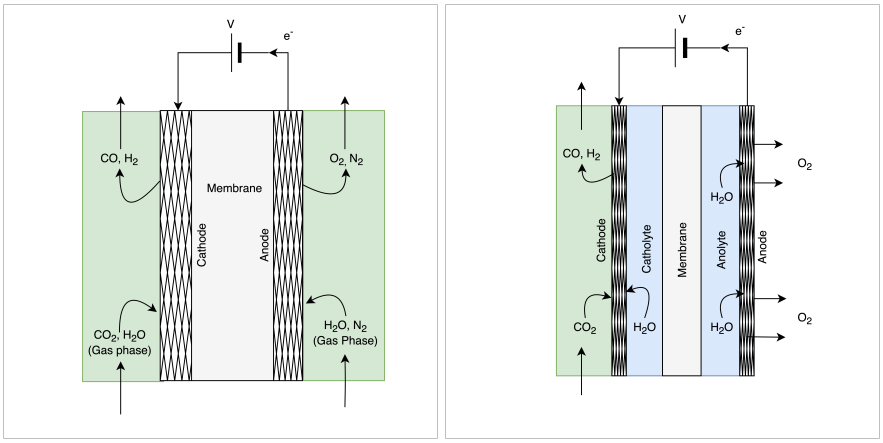

(a) Schematic of gas-phase electrolyser (b) Schematic of liquid-phase electrolyser

Figure 1.3: Flow cell designs for CO_2 Electrolysis

In liquid-phase electrolyser, as shown in Figure 1.3b, a supporting electrolyte flows between the membrane and the electrode. The presence of the electrolyte allows for controlling and optimising the reaction environment but increases the solution resistance leading to an increase in ohmic losses and low energy efficiency. High current density up to $1000\left(\frac{mA}{cm^2}\right)$[9] were reported, but these assemblies were short-lived due to flooding of the electrolytes into the gas-phase. In gas-phase electrolyser, as shown in Figure 1.3a, by embedding the catalyst on the membrane to transport ions, solution resistances are removed. It is also called a zero-gap assembly. Current densities ranging from $100 - 440\left(\frac{mA}{cm^2}\right)$ were reported in this assembly owing to enhanced mass transfer [9–11, 20–23]. Gas-phase electrolysers are also stable and can be used for long-term operations. But the gas-phase needs to be humidified to hydrate membrane and thus making gas-phase electrolysers difficult to scale-up, control and optimise[9].

There are also other innovative cell designs such as membrane-less microfluidic flow cells. Ohmic losses are minimised due to their small size in microfluidic flow cells, but the production rates are meagre. Although liquid-phase electrolysers show high current densities, they are unstable and uses corrosive electrolyte solutions, making them very difficult to scale-up as well[24]. At present, liquid-phase,

electrolysers have the best performance but are *yet to reach the required metrics* for commercialisation.

1.2. Problem Description

It is clear from the section 1.1, there are three main barriers for commercial realisation of CO_2 electrolysis: Transport limitations, Low solubility of CO_2, Continuous supply of CO_2 and H_2O. There were different solutions to deal with the above challenges, but none were successfully able to address all of them. Liquid-phase electrolysers came close but are limited to laboratory scale due to their complexity and energy losses. In this thesis, we propose a solution which can address all 3 challenges by making use of two-phase flow that is inherent to CO_2 electrolysis. The idea is to create Taylor flow to enhance the mass transfer and thus the performance of the flow cell. We envision a system as shown in Figure 1.4.

The relation between hydrodynamics, mass transfer and electrochemistry becomes apparent by looking at the limiting current density. Limiting current density is, the total current density at which the process is limited by mass transfer. For the simplest case the limiting current density, from Faraday's law and film theory, is given by

$$\frac{j_{lim}}{nF} = \nu_m \approx \frac{DC^o}{\delta} \tag{1.4}$$

where j_{lim}, ν_m are the limiting current density and mass transfer rate respectively. D, C^o are the effective diffusion coefficient and the saturated concentration of CO_2 in water and $\delta\ (m)$ is the diffusion layer thickness. From Equation 1.4, the mass transfer can be increased by decreasing the diffusion layer thickness (δ), increasing the solubility of CO_2 in water or increasing the diffusion coefficient.

In Taylor flow, the diffusion layer lies in the film between the gas bubble and the electrode surface and can be varied precisely by changing the flow conditions. In a laboratory H-cell with good mixing, the diffusion layer thickness is of the order of $50\ \mu m$. In the Taylor flow, this thickness can easily be made $1\ \mu m$ by adjusting the flow conditions, which is already showing an order of magnitude improvement in mass transfer. The flow bubbles provide a continuous supply of CO_2 and H_2O without being limited by the CO_2 solubility. In addition to improved mass transfer, with setup, as shown in Figure 1.4, the ohmic losses are also kept to minimum similar to gas-phase electrolysers. Unlike gas-phase electrolysers, the membrane is hydrated continuously, and controllability is not lost.

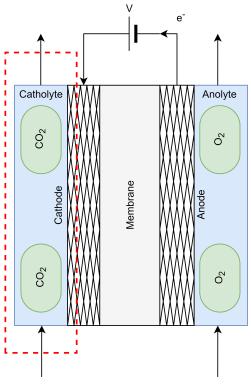

Figure 1.4: Flow cell design with Taylor Flow

The hypothesis for this thesis is:

Taylor flow with its enhanced mass transfer improves the performance of CO_2 electrolysis

Although the concept of Taylor flow to enhance the electrolysis seems viable and attractive, much is not known about this system, and there is no prior work where Taylor flow is analysed in an electrolyser. As a starting point, reactive systems, in which Taylor flow is investigated, are considered from literature. A similar system with only the cathode side of the electrolyser is considered, with an electrochemical reaction occurring at the flow-electrode interface instead of a chemical reaction. Figure 1.4 shows the region of interest in the red box. The hypothesis is assessed by developing a model and solving it numerically using COMSOL Multiphysics®. COMSOL is selected as it has a well-developed interface for solving equations involving electrochemical reactions and integrate a variety of physics.

1.3. Research Questions

Based on the above problem description, the objective of this thesis is "*to numerically investigate the performance of CO_2 electrolysis due to Taylor flow*" and the following research questions were formulated to achieve it:

1. What range of current densities and efficiencies can be achieved using Taylor flow?
2. How does the flow conditions such as liquid or gas velocities affect the production rate of the flow cell?
3. How does bubble dissolution affect the flow cell metrics

The modelling approach and theory were discussed in chapter 2 and chapter 3

1.4. Thesis Outline

Chapter 2 explains the approach used in the thesis and discuss the design of the computational domain. Chapter 3 provides a summary of the theoretical concepts that are necessary to understand the nuances of this report and develop models based on the strategy from Chapter 2. Chapter 4 focuses on numerical investigation and model validation. Chapter 5 discusses the results of the model developed. Chapter 6 concludes the report with highlights and future outlook relevant to experimental and modelling studies.

2

Design

Performance of electrochemical flow cell, as discussed in section 1.2, depends on the interplay among hydrodynamics, mass transfer, ion transport, chemical reactions in bulk and at the surface. An electrochemical model involves these complex web of interactions and often results in a system with too many degrees of freedom to solve. For a proper understanding of the process, it is necessary to unwind these interactions by simplifying the system through certain assumptions. The assumptions are made such that the model is still able to answer the research questions of interest within acceptable limits. In this chapter, the author would like to describe the strategy and design for the computational study.

2.1. Strategy

In the Electrochemical flow cell, as shown in Figure 1.4, CO_2 is transported from the bubble to the cathode through water, where it undergoes reduction on an Ag catalyst to form CO and OH^- . The produced Hydroxyl ions (OH^-) are transported through an anion exchange membrane to the anode, where they undergo oxidation reaction to produce Oxygen (O_2). Anode, membrane and cathode are coupled with the mass transport in addition to the applied external potential. Since the interest of this thesis is to understand the effect of transport of CO_2 on the performance of electrolyser, it is sufficient to analyse the cathode side (red box) of the electrolyser as shown in Figure 1.4.

The author made two assumptions to the cathode side of the electrolyser independently from the anode. First, a reference electrode of known standard potential is assumed to be present close to the cathode. This setup is called a 3-electrode system which is commonly used in voltammetric studies[25]. With this setup, the electrode potential at the cathode is known and can be directly related to the applied potential. Secondly, OH^- ions are assumed to be transferred through the membrane instantaneously, making the surface reaction at the cathode solely a

function of overpotential at the cathode and transport of reactants. These assumptions decouple the cathode side of the CO_2 electrolyser from the membrane and anode and simplify the modelling of a complex electrochemical cell into the modelling of Taylor flow in the cathode channel with an electrochemical surface reaction.

In Taylor flow, a long train of bubbles almost filling the capillary moves in the fluid at regular intervals, as shown in Figure 2.1. Due to the periodicity of the bubbles, a single bubble with 2 liquid slugs with half the slug length on either side, from here on referred to as a unit cell, can be considered a representative of the flow. A modelling strategy which uses unit cell was first introduced by Edvinsson and Irandoust [26] and later used by other researchers to successfully characterise hydrodynamics[27–30] and mass transfer[31–34] under various operating conditions. In this thesis, a similar strategy was used, extending it to CO_2 electrolysis.

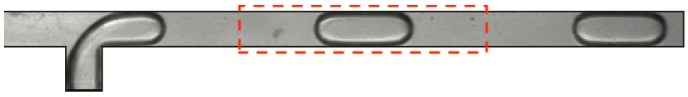

Figure 2.1: Taylor Flow[35]

In the unit cell approach, choosing bubble frame of reference fixes the computational domain. It is equivalent to observing the bubble as it's moving along the length of the channel. As shown in Figure 2.1, the unit cell (red box) consists of two-phases: gas and liquid. In CO_2 electrolysis, most of the phenomena happen in the liquid phase. Thus for practical considerations, the physics inside the gas bubble is of less importance and can be ignored with the right set of boundary conditions. By ignoring the gas phase, the complex multiphase flow problem is reduced to a single-phase laminar flow problem. Therefore, using the unit cell approach decreases the complexity of the model as well as the computational costs. The numerical analysis uses a quasi-steady-state analysis, which neglects the change in bubble size in the time scale of processes that lead to an electrochemical reaction. The bubble thus becomes part of the geometry, and a parametric study of bubble size can provide information on transient behaviour.

2.2. Geometry

The unit cell contains a CO_2 bubble moving with velocity u_B alongside the water in a circular microchannel. The electrolyser design assumes that the electrochemical catalyst is spread uniformly around the channel. Figure 2.2 shows the shape of the unit cell for circular capillary in 2D. The diameter of the channel, length of bubble and slug phase, the shape of the bubble should be known to determine the shape of the unit cell. Bubble shape is determined by mean curvature radius κ, which depends on the surface tension between water and CO_2 and normal stresses acting on the interface. In multiphase flow, inertial forces and gravitational forces provide normal stresses and are assumed to be negligible to simplify the geometry. This assumption is valid for small bubble velocities and channel diameters[30]. In the

absence of these forces only viscous forces prevail in the liquid and bubble tries to take the shape of an elongated sphere as shown in Figure 2.2[36]. The diameter of the bubble can be determined based on the thickness of the liquid film (δ) left behind by the bubble.

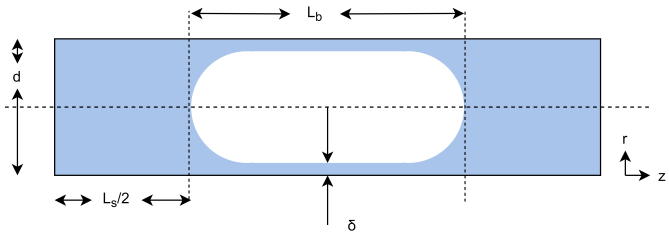

Figure 2.2: Computational domain(blue) for the simulation. L_b is the length of the bubble from one end to the other end of the cap

The liquid film thickness is determined through well-established correlations from literature[27, 36, 37]. The empirical relation provided by Aussillous and Quere [37] is:

$$\frac{\delta}{d} = \frac{0.66Ca^{2/3}}{1 + 3.33Ca^{2/3}} \tag{2.1}$$

where $Ca = \frac{\mu u_B}{\sigma}$ is the capillary number. Equation 2.1 was valid for all ranges of capillary numbers tested experimentally for high-viscous fluids but starts deviating for low-viscous fluids such as water and ethanol[28, 37] after certain Capillary number(Ca^*) indicating a regime change where inertial forces are becoming significant. Aussillous and Quere [37] found through scaling analysis that the limiting capillary number (Ca^*) is given by $Ca^* = \left(\frac{2\mu^2}{\sigma\rho d}\right)^{\frac{3}{4}}$. It is clear from Ca^* that small channel diameters provide the largest range for Capillary numbers for which Equation 2.1 is valid. Accordingly a channel size of 100μm is chosen. Any parametric study involving diameter is varied in the same order of magnitude($O(10^{-4})$).

Finally to complete the geometry, bubble (L_b) and slug (L_s) lengths need to be specified. They can be be obtained from the unit cell length, L_{uc} and void fraction, $\epsilon_b = \frac{L_b}{L_{uc}}$. Research by Shao et al. [29], Van Steijn [35] showed that the unit cell length depends on the ratio of superficial gas and liquid velocities ($\frac{u_{GS}}{u_{LS}}$) while the void fraction depends on the inlet conditions such as having a T or Y-junctions to create the slugs.The average velocity of the liquid, u_{TP} is given as $u_{GS} + u_{LS}$. The ratio of superficial velocities and inlet conditions adjust the desired unit cell length and void fraction for a given liquid velocity. Thus it is assumed that they can be changed independently from flow conditions and are provided as inputs to the system. Using the unit cell approach developed in section 2.1 and geometry from section 2.2 modelling of the electrochemical cell is described in chapter 3.

3

Modelling

3.1. Electrochemical Model

The present work uses a unit cell strategy, as explained in chapter 2 and considers a two-dimensional model to describe the electrochemical cell by exploiting the axis-symmetry. The purpose of this model is to gain insights into the transport in Taylor flow and assess its role in CO_2 electrolysis. This strategy allows integrating the discreet nature of bubbles and liquid slugs in a continuum model by simplifying the multiphase flow into single-phase transport problem. Transport phenomena, in general, are classified into three types: Mass, Momentum and Energy transport. For microchannels with their high specific surface area, it is reasonable to assume that the process is isothermal. This assumption excludes the energy balance from model equations. Mass transport, which includes overall mass balance and conservation of individual species (Species Transport), Momentum transport (Hydrodynamics) and Electrochemistry, are discussed in this section.

Figure 3.1 shows the schematic representation of a unit cell with defined boundaries in bubble frame of reference. For simplicity, a cylindrical coordinate system is chosen. The bubble supplies the reactant CO_2, which is transported through the water to the wall to react and produce CO.

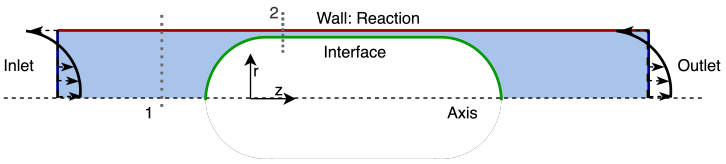

Figure 3.1: A schematic representation of 2D unit cell with ECR at wall in bubble frame of reference

The transport of species should follow mass conservation, such that

$$\frac{\partial c_i}{\partial t} = -\vec{\nabla}.J_i + R_{i,b} \tag{3.1}$$

here, J_i, c_i are the molar flux and concentration of species "i" (CO_2, CO) respectively and $R_{i,b}$ is the volumetric homogeneous reaction rate. For an electrochemical system, the molar flux of the species can be expressed in terms of 3 different fluxes: Diffusion, Convection and Migration. Migration is absent as species that are examined are neutral and the flux is written as sum of diffusion and convective fluxes.

$$J_i = -D_i\vec{\nabla}c_i + \vec{u}c_i \tag{3.2}$$

where D_i is the binary diffusion coefficient of species "i". It is assumed that the solution is dilute so that the interaction between the species and the variation in diffusion coefficients can be neglected. The velocity of liquid, $\vec{u}$, depends on flow dynamics and is obtained from momentum balance.

The volume-averaged momentum balance and mass balance for an incompressible Newtonian fluid are given by Navier-Stokes and continuity equation, respectively.

$$\rho\frac{\partial\vec{u}}{\partial t} + (\rho\vec{u}).\vec{\nabla}\vec{u} = -\vec{\nabla}P + \mu\nabla^2\vec{u} + \cancelto{0}{F_b} \tag{3.3}$$

$$\vec{\nabla}.\vec{u} = 0 \tag{3.4}$$

where $\vec{u}$, ρ, μ, represents the velocity vector, density and viscosity of the liquid respectively. P is the pressure, and F_b represents the body forces acting on the liquid such as gravity. It is assumed that the body forces are absent or insignificant. Note that the hydrodynamic Equations 3.3 and 3.4 can be solved independently from species transport to determine velocity $\vec{u}$ which can later be used in Equation 3.2 to determine species concentrations. The obtained set of partial differential equations need boundary conditions to solve.

3.1.1. Boundary Conditions

The interface between bubble and liquid is treated as free surface and the saturated concentration, C_i^o, is obtained from Henry's law such that $C_i^o = H_i P_B$. Here H_i, P_B are Henry's constant and pressure inside the bubble. At inlet and outlet, the periodic boundary condition assumes that the concentration and fluxes of species are the same. This condition is not true as the concentration changes along the length of the channel due to the reaction at the wall. Van Baten and Krishna [33] modelled wall mass transfer in Taylor flow and showed that this boundary condition only leads to an error of 0.3% in the final results in return for the reduced computational effort. The Hagen-Poiseullie parabolic velocity profile at inlet and outlet ensures that the mass is inherently conserved[28]. As the bubble moves along the channel, it pushes the liquid slugs along its way. Thus the average liquid velocity, u_{TP} and bubble velocity, u_B are dependent on each other. The relation between them is

determined by writing the mass balance over cross-sections 1 and 2 in Figure 3.1.

$$\rho A_S(u_{TP} - u_B) = \rho A_F(u_F - u_B) \tag{3.5}$$

where A_S, A_B, A_F are cross section areas of liquid slug, bubble and film respectively. u_F is the average velocity inside the film. Since the cross sectional area of the film, A_f, is much smaller than $A_S \& A_B$, the contribution of the film volumetric flow is assumed to be negligible in Equation 3.5. This assumption is called stagnant film assumption[1] and is frequently used in literature[33, 34, 38–41]. This implies $A_S u_{TP} = A_B u_B$. Substituting expressions for $A_S \& A_B$, Equation 3.6 can be easily derived. The film thickness (δ) is calculated using Equation 2.1. Finally, to complete the model, the surface reaction rate, $R_{i,s}$, needs to be determined which depends on the electrochemical reaction kinetics.

$$\frac{u_{TP}}{u_B} = 1 - \frac{4\delta}{d} \tag{3.6}$$

The boundary conditions are summarised in Table 3.1.

Table 3.1: Boundary conditions for 2D Model

Boundary	Hydrodynamics	Species Transport
Inlet	$\vec{u} = 2u_{TP}\left(1 - \left(\frac{r}{R}\right)^2\right) - u_B\hat{z} + 0\hat{r}$	Periodic Boundary Condition
Outlet	$\vec{u} = 2u_{TP}\left(1 - \left(\frac{r}{R}\right)^2\right) - u_B\hat{z} + 0\hat{r}$, $P = 0$	Periodic Boundary Condition
Interface	Slip condition, $\mathrm{T}.n = 0$ - Free surface	$c_i = C_i^o$
Wall	No slip, $\vec{u} = -u_B\hat{z} + 0\hat{r}$	$-D_i\nabla_n c_i = -R_{i,s}(\eta)$

Electrochemistry Any general electrochemical red-ox reaction involving oxidising (Ox) and reducing agents (Red) can be written as:

$$\mathrm{v_O\,Ox} + n\,\mathrm{e}^- \rightleftharpoons \mathrm{v_R\,Red}$$

In electrochemical systems, the current densities are measured against certain potentials. Current densities represent charge transfer rates at the electrode surface and can be related to reaction rates using Faraday's law.

$$R_{i,s}(\eta) = \frac{-\nu_i j(\eta)}{nF} \tag{3.7}$$

where j is the current density at the electrode. The negative sign is used to account for the convention that the current at the cathode is negative. Initially, in an open circuit, the reactions are at equilibrium, and there is no net current at the electrode

[1] For the extensive list of all the assumptions made, refer to Appendix A

surface. The equilibrium electrode potentials that are called formal potentials ($E^{o'}$) are available in the literature for various reactions at standard conditions. For systems far from standard conditions, the Nernst equation is used to determine the equilibrium potential, which includes the effects of concentration. It is given by:

$$E_{eq} = E^{o'} - \frac{RT}{nF} ln \frac{C_{R,S}^{\nu_R}}{C_{O,s}^{\nu_O}} \tag{3.8}$$

where $C_{i,S}$ are the surface concentrations at the electrode and E_{eq} is the equilibrium potential at the electrode. To move the reaction forward from equilibrium, a potential greater than the equilibrium potential needs to be applied. This is analogous to activation energy from chemical kinetics[42]. The additional potential that drives the reaction is called as overpotential (η) and is defined as $E_A - E_{eq}$ where E_A is applied electrode potential. Therefore, the reaction rate depends on the overpotential together with concentration at the electrode surface. Different experimental studies showed that the dependence of rate on overpotential is exponential in nature[25] and the concentration-overpotential equation describing first-order electrode kinetics is given by Equation 3.9. If there are no mass transfer effects then the Equation 3.9 simplifies to the famous Butler-Volmer kinetics.

$$j(\eta) = -j_o \left(\frac{C_{O,s}}{C_{O,b}} e^{\frac{-\alpha_c F \eta}{RT}} - \frac{C_{R,s}}{C_{R,b}} e^{\frac{\alpha_a F \eta}{RT}} \right) \tag{3.9}$$

Here j_o is called exchange current density. It quantifies the system's ability to reach the desired current density with minimum losses[25, 43]. $C_{i,b}$ are bulk concentrations when the reactions are at equilibrium, and α_c, α_a are transfer coefficients for cathode and anode respectively. For the case of CO_2 electrolysis, CO is produced only at negative potentials, and thus only cathodic current is significant, and Equation 3.9 becomes:

$$j(\eta) = -j_{o,CO_2} \left(\frac{C_{CO_2,S}}{C_{CO_2}^o} e^{\frac{-\alpha_c F \eta_{CO_2}}{RT}} \right) \tag{3.10}$$

Substituting Equation 3.10 in Equation 3.7, the surface reaction rate simplifies to Equation 3.11, similar to a first order reaction from chemical kinetics. Using Equation 3.11 in the wall boundary condition, the model for the electrochemical cell with Taylor flow is fully specified.

$$R_{i,s} = \nu_i k(\eta) C_{CO_2}, \quad k(\eta) = \frac{j_{o,CO_2}/nF}{C_{CO_2}^o} e^{\frac{-\alpha_c F \eta_{CO_2}}{RT}} \tag{3.11}$$

3.1.2. Quasi-Steady-State Analysis

In the current study, CO_2 for the electrochemical reaction is supplied continuously through the bubbles. The bubbles dissolve as the CO_2 gets converted at the cathode. The dissolution also affects the mass transport in the system because of the change in the interfacial surface area. The bubble dissolution and its effects are

modelled through a quasi-steady-state analysis. The quasi-steady-state approach assumes that the mass transfer processes, i.e. convection and diffusion, occur at a faster rate and thus achieve a steady-state before the effect of changing bubble size is observed. This assumption is valid when the time scale in which bubble shrinks is much larger than the convection and diffusion time scales and is further discussed in chapter 5. The rate at which bubble dissolves is then calculated using the flux at the interface, J_{I,CO_2}, and is given by Equation 3.12.

$$-C_B \frac{dV_B}{dt} = \int_{A_I} (J_{I,CO_2}.n) dA \tag{3.12}$$

where C_B is the concentration of CO_2 inside the bubble with a volume V_B. The bubble concentration is determined from ideal gas law. The flux at the interface is obtained from the steady-state solution of the electrochemical model for a fixed bubble size. Discrete-time intervals are chosen assuming the bubble volume is unchanging in these intervals. Various bubble sizes are calculated in a discrete manner using Equation 3.12. The electrochemical model is then solved in each interval, i.e. for each bubble size to understand the effect of bubble dissolution on mass transfer in Taylor flow.

3.2. Finite Element Method

The current work uses the commercial software, COMSOL Multiphysics ® to solve the pde's obtained in section 3.1. COMSOL uses the Finite Element Method (FEM) to convert the equations into a system of algebraic equations, which are favourable to solve using numerical methods. This section discusses the FEM method briefly to understand the nomenclature used in chapter 4.

In FEM, to determine the solution, the domain of interest is first divided into several sub-domains called elements. The elements can be of various shapes. For a 2D system, triangular or quadrilateral shapes are commonly used [44]. A set of functions called as shape functions are developed such that they approximate the exact solution in each element. The shape functions of each element are then assembled over the entire domain such that the boundary conditions and continuity between each element are maintained. Numerically, the shape functions are determined using *the method of weighted residuals*. In this method, the shape function is approximated as a combination of *test functions* whose coefficients are unknown. Lagrangian interpolating polynomials are commonly used as shape functions[44]. Unknown variables are defined at each node and forces the resultant shape function to satisfy the governing equations. Naturally, errors or residuals arise in each element, and the coefficients of the shape function are determined such that it minimises the weighted average of residual over the domain. If the choice for weights is the test functions, then this approach is called a Galerkin approach, and COMSOL Multiphysics ® implements it by default. Increasing the number of elements by refining the mesh, increases the number of shape functions and therefore, improves the solution accuracy but comes at the expense of computational cost.

4

Simulation

Simulations are performed in COMSOL Multiphysics®, to solve the partial differential equations developed in section 3.1. In this chapter, section 4.1 discusses the organisation of the simulation studies, highlighting the numerical parameters, mesh features and solver settings. section 4.2 discusses the results from the mesh sensitivity study, performed to verify that the simulations obtain an unchanging solution. Later, the simulation results are validated with theoretical models and experimental results from the literature to derive useful conclusions, later from the results.

4.1. Organisation

In the electrochemical model from section 3.1, the hydrodynamics can be resolved independently from the species transport. Therefore, the simulations first solve the hydrodynamic equations for the velocity profile. The velocity profile is then used in species transport to calculate the concentration profile. This approach is implemented in COMSOL using predefined physics interfaces. The physics interfaces are fundamentally a set of generic partial differential equations grouped based on specific applications. The electrochemical model uses the laminar flow and electroanalysis interface from COMSOL. The laminar flow interface consists of equations related to hydrodynamics, i.e. Navier-Stokes and continuity equation. The electroanalysis interface has equations related to dilute mass transport of species through convection, diffusion and migration and has a particular boundary condition to specify electrochemical kinetics at a boundary. Boundary conditions summarised in Table 3.1 are used in COMSOL to complete the model. The block diagram, with blocks representing the interfaces from COMSOL Multiphysics, as shown in Figure 4.1, shows the input/output representation of the electrochemical model.

Table 4.1 compiles the values of geometry and process parameters given as model inputs in the simulation. The range of velocities is chosen such that the inertial forces remains low (Re<100), and the flow doesn't affect the shape of the

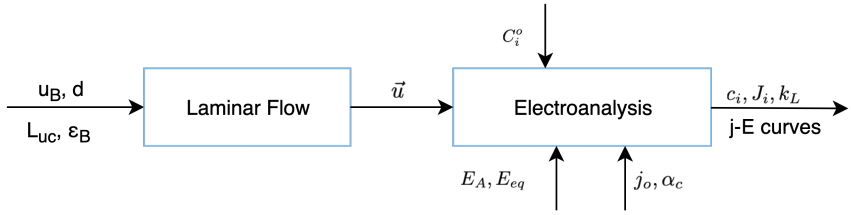

Figure 4.1: Block Diagram for 2D Model

bubble[27, 36, 37, 39]. The parameters for electrochemical kinetics, i.e. j_o, α_c, are taken from the research work by Wu et al. [45]. Wu et al. [45] determined kinetic parameters for electrochemical reduction of CO_2 to CO in a microfluidic-liquid phase electrolyser, by fitting the Butler-Volmer equation with their experimental results. It is assumed that these kinetics still holds for the system with Taylor flow. In reality, this assumption might not be valid as the kinetic parameters are system-specific and are dependent on the local reaction environment such as pH[12]. However, this assumption only causes errors in the absolute values, and the relative trends should remain the same. Table 4.2 lists the physical constants for CO_2 – CO – H_2O system used in the simulations.

Table 4.1: Inputs for the 2D model

Parameter	Value
Diameter (d)	100-400 μm
Unit cell Length (L_{uc})	5×d μm
Void Fraction (ϵ_B)	0.33-0.67
Bubble Velocity (u_B)	0.004 - 0.4 $m.s^{-1}$
Equilibrium potential (E_{eq})	0.52 V
Applied Potential (E_A)	0.5 V - 3.6 V
Cathode Transfer Coefficient (α_c)	0.17 [45]
Exchange Current density (j_o)	0.091 $A.m^{-2}$ [45]

Table 4.2: Physical constants for the 2D model

Physical Constant	Value
Density (ρ)	1000 $kg.m^{-3}$
Dynamic viscosity (μ)	8.9e-4 $Pa.s$
Surface tension (σ)	0.072 $N.m^{-1}$
Saturated concentration, CO_2 ($C^o_{CO_2}$)	34 $mol.m^{-3}$
Reference concentration, CO_2 ($C^{Ref}_{CO_2}$)	40.9 $mol.m^{-3}$
Diffusion coefficient, CO_2 (D_{CO_2})	1.9e-9 $m^2.s^{-1}$
Saturated concentration, CO (C^o_{CO})	1 $mol.m^{-3}$
Diffusion coefficient, CO (D_{CO})	2.1e-9 $m^2.s^{-1}$

Please note: The electrochemical model is non-dimensionalised to avoid small numbers which lead to numerical errors and convergence problems. Appendix D reviews the model equations in non-dimensional form.

4.1.1. Meshing

Finite Element Method (FEM), as mentioned in section 3.2, is used by COMSOL to determine a solution numerically. Therefore, meshing is performed to discretise the domain of interest into smaller domains. The present work uses a user-controlled mesh built with unstructured quadrilateral(quad) elements. The unstructured mesh is used as the domain has sharp corners and curved boundaries, and quadrilateral elements are preferred to triangular elements as they improve convergence in flow simulations[46]. CFD studies by Gupta et al. [47], Fletcher and Haynes [48] recom-

mend that the film region should contain at least five elements to capture details of flow around the bubble. Therefore, by adjusting the growth rate and element size, the film region is also sufficiently resolved with more than five elements along the radius. The mesh is then optimised to create a finer mesh close to the wall, bubble interface and axis where high concentration gradients are expected. Figure 4.2 shows the resultant mesh.

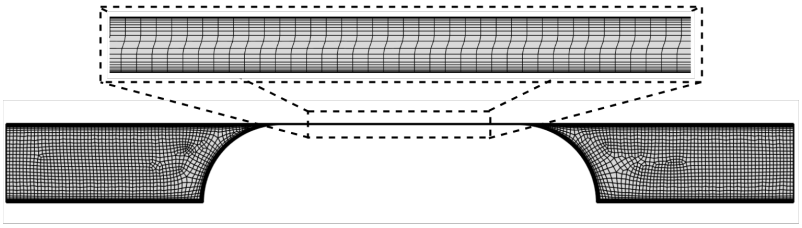

Figure 4.2: Fine mesh for the electrochemistry model

A mesh-independent study, with four meshes, is carried out to determine the optimal mesh and to obtain a precise solution. Table 4.3 summarises the details of meshes used for sensitivity study. subsection 4.2.1 discusses the sensitivity study results Also, to achieve higher solution accuracy, piece-wise linear interpolation (P1) for pressure, quadratic interpolation (P2) for velocity components and cubic polynomial interpolation(P3) for concentrations are used for shape functions in each element. The choice is made based on the recommendations made by Durán Martínez et al. [49] where they investigate mass transfer in Taylor flow, with a first-order reaction at the wall.

4.1.2. Studies and Solvers

The electrochemical model is studied using a quasi-steady-state approach, as discussed in subsection 3.1.2. Therefore, a stationary solver which solves the steady-state equations is selected in COMSOL. COMSOL, using FEM, converts the partial differential equations from the electrochemical model into a set of linear algebraic equations of the form $K.x = f$ for each element. K is called a stiffness matrix, x is a column vector of unknowns at every node and F comprises of external influences applied on the nodes. There are two sets of algorithms, in COMSOL, to solve for $x = K^{-}1.f$: direct and iterative solvers. Direct solvers are solvers based on the LU decomposition algorithm and solve the system of equations in a single step.[44, 50]. Iterative solvers use search algorithms similar to the conjugate gradient method to arrive at a solution gradually[44, 50]. The simulations in this thesis use the direct solvers as they are easy to implement and give robust solutions.

Please note: All simulations are performed on a computer with Dual-Core Intel i5 processor; 2.9GHz processor speed; and 8GB RAM.

4.2. Validation

Validation of the electrochemical model is done in two phases. First, mesh independent studies are performed to verify the solution convergence. Later, the model results are tested with the experimental results and some theoretical models from literature to show that the electrochemical model can accurately simulate the desired physics and make meaningful interpretations from the results. Following the workflow from section 4.1, the results are sub-divided into two classes: Hydrodynamics and Electroanalysis. The results from hydrodynamics are first validated to obtain *proper* velocity profiles. Later, electroanalysis results are confirmed.

4.2.1. Mesh Independent Study

Four different meshes with the increasing resolution are chosen for mesh sensitivity study, and the relevant details are listed in Table 4.3. Note that the mesh parameters depend on the bubble velocity, u_B as the film thickness changes with it—subsequently, the domain. Thus a bubble velocity of 0.04 $m.s^{-1}$, which is in the middle of the range, is chosen from the list of process parameters. Relative tolerance of *1e-3* is set for achieving convergence. For hydrodynamics, the velocity profiles inside the film and liquid are observed. For electroanalysis, the local current density at the cathode and the concentration profile of CO_2 in the liquid slug is observed. Figure 4.3 and 4.4 shows the results, respectively.

Table 4.3: Mesh details for mesh independent study, $u_B = 0.04 m.s^{-1} s$

Mesh Parameter	Coarse	Fine	Finer	Finest
No. of elements	19386	33945	74428	135812
No. of Elements in film	12	19	22	38

As seen from Figure 4.3a, the velocity profiles in the film region for different meshes superimpose. This shows that the film region is sufficiently resolved for selected meshes when the number of elements along the radius exceeds ten. Figure 4.3b shows the magnitude of velocity in the liquid slug. As seen from the highlighted

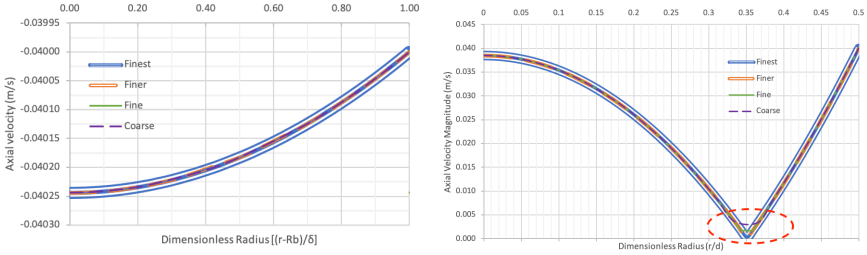

(a) Velocity profiles in film for different meshes. (b) Velocity profiles in liquid slug for different meshes.

Figure 4.3: Results from mesh independent study for hydrodynamics. $u_B = 0.04 m.s^{-1}$, $d = 100 \mu m$

region (red-dotted circle) in the figure, the dead zone, i.e. the position at which

the velocity becomes zero is poorly resolved by the coarse and the fine mesh. On the other hand, the finer and finest mesh correctly determines the location of the vortex centre.

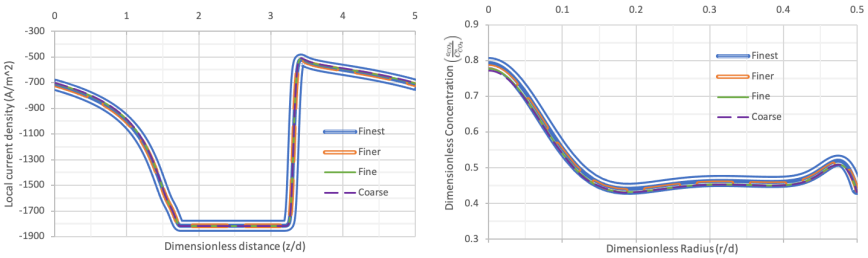

(a) Local current density at cathode for different mesh sizes

(b) CO_2 concentration profile in liquid slug for different meshes

Figure 4.4: Results from mesh independent study for electroanalysis. $E_A = -2V, L_{uc} = 500\mu m$

The reduced accuracy of the coarse and fine mesh doesn't extend to the electroanalysis results, as shown in Figure 4.4a and 4.4b[1]. The numerical improvement is due to the higher-order discretisation used for concentrations in COMSOL. A maximum error of less than 1% was determined for the vortex position, average current density, and average concentration among the chosen meshes. Notably, the finer mesh becomes computationally expensive for smaller bubble velocities. Thus, parametric studies involving velocity use the fine mesh while all other analyses are done on the finer mesh.

4.2.2. Hydrodynamics

Slug Velocity Profile For Taylor flow in circular capillaries, the cross-talk between the liquid slugs occurs through the film. Only a small portion of the liquid is transferred through the film and rest of the fluid circulates between the bubbles creating the well-known vortices[28, 39, 51]. The position at which the velocity of the liquid becomes zero is the vortex centre. Thulasidas et al. [39] conducted experiments to determine the vortex centre as a function of capillary number(Ca_B). Analytically, the vortex centre is derived from the Hagen-Poiseullie parabolic velocity profile inside the liquid slug. The parabolic velocity profile is written as $\vec{u} = 2u_{TP}\left(1 - \left(\frac{r}{R}\right)^2\right) - u_B$. Equation 4.1 gives the expression derived from the parabolic velocity profile.

$$\frac{R_v}{d} = \frac{1}{2\sqrt{2}}\sqrt{2 - \Psi} \tag{4.1}$$

where, $\Psi = \frac{u_B}{u_{TP}}$. The velocity profile inside the liquid slug is validated by comparing the simulation results with the experimental work of Thulasidas et al. [39] and the analytical expression given by Equation 4.1. Figure 4.5 shows the outcome.

[1]Enlarged version of the mesh independent plots are in Appendix F

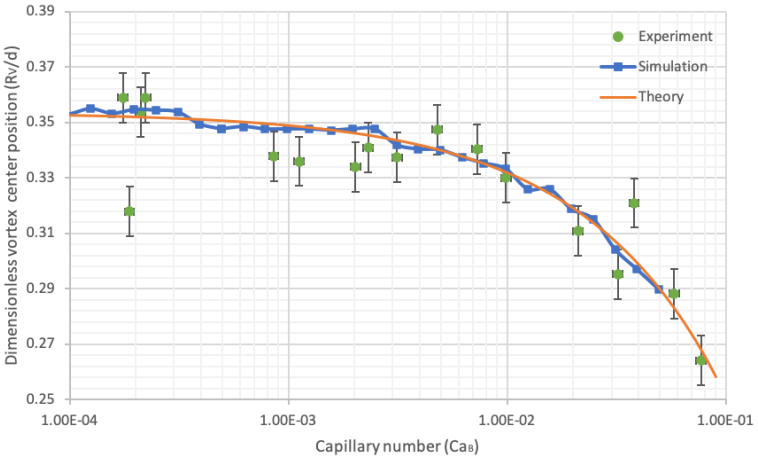

Figure 4.5: Vortex center (R_v) position as a function of capillary number($Ca_B = \frac{\mu u_B}{\sigma}$), Error bars represent standard errors

Figure 4.5, uses a logarithmic scale on the x-axis, and the "Theory" curve is the analytical expression. Equation 3.6 calculates the value of Ψ using the stagnant film assumption. From the figure, it is clear that the vortex centre from the electrochemical model matches closely with the analytical expression. The oscillations of the simulations results around the theoretical line are due to the use of the fine mesh for the parametric study instead of the finer mesh. The choice leads to an error of 1% only. The results also match reasonably well with the experimental results, with a standard error of 3%. This analysis verifies that the stagnant film assumption is valid for the tested set of capillary numbers, and the right set of equations are modelled for the hydrodynamics.

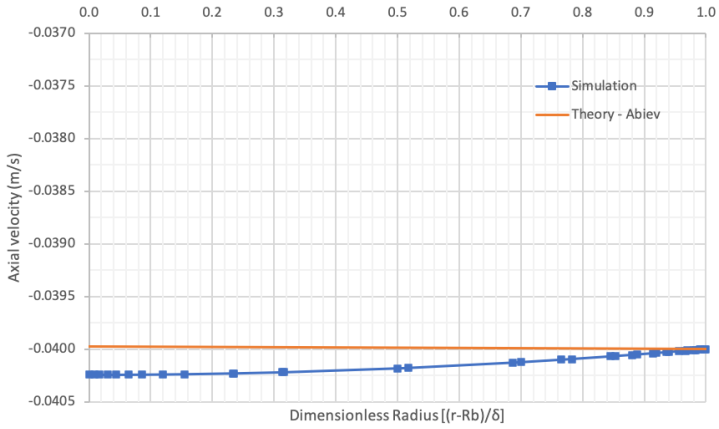

Figure 4.6: Velocity profile in film region. $u_B = 0.04 m.s^{-1}$

Film Velocity Profile Abiev [52] developed a theoretical model to determine velocity profiles in the bubble, liquid slug and the film. In the present work, the theoretical model is solved in Matlab[2] to determine the velocity profile inside the liquid film. The solution is then compared with the results from the hydrodynamic simulations in COMSOL. Figure 4.6 shows the outcome. The model by Abiev predicts a plug flow behaviour inside the film. The solution from the electrochemical model deviates slightly from the theoretical solution with a small error of 0.75% only. Hence, the velocity profile in the film region is verified. With both the velocity profiles in film and slug regions verified, the hydrodynamics is successfully validated.

4.2.3. Electroanalysis

Electrolysis using Taylor flow is a novel concept, and therefore the literature available in this subject are meagre, and experimental validation is not possible. Much of the literature is available for reactive systems such as monolith reactors with Taylor flow[27, 33, 41, 49, 53]. Unfortunately, none of them applies to the current work as they operate with channel sizes greater than one mm and Reynolds number higher than 100, where gravitational and inertial effects are not negligible. Therefore, current work follows a different approach in which the electrochemical model is solved and verified for the laminar pipe flow instead of Taylor flow.

In the laminar-pipe-flow cell[3], the saturated solution of CO_2 is supplied continuously through a circular capillary. The wall of the capillary acts as a cathode where CO_2 electrolysis occurs. The electrode potential is increased to reach a limiting current density. In this situation mass transport, limited by diffusion, forms a concentration boundary layer called a Nernst diffusion layer. This situation is similar to the classical Graetz problem[54], where a developing concentration boundary layer and fully-developed flow are assumed. The solution to the Graetz problem leads to the expression for diffusion layer thickness(δ_N) and is given by Equation 4.2.

$$\frac{\delta_N}{d} = 1.022\sqrt[3]{\frac{D_{CO_2} z}{u_{TP} d^2}} \tag{4.2}$$

For the derivation of the Equation 4.2, the reader is referred to the book written by West [42]. The solution to the Garetz problem is obtained by solving the transport equations discussed in the electrochemical model. Therefore, the same transport equations from the model are solved in COMSOL for pipe flow, using the same electrochemical kinetics from Table 3.1 and appropriate inlet and outlet boundary conditions. The boundary layer thickness is then measured to compare with the theoretical value given by Equation 4.2. Figure 4.7 shows the outcome.

[2] Matlab code for the film profile can be found in Appendix C

[3] Details regarding the simulation settings, boundary conditions for the laminar-pipe-flow cell can be found in Appendix B

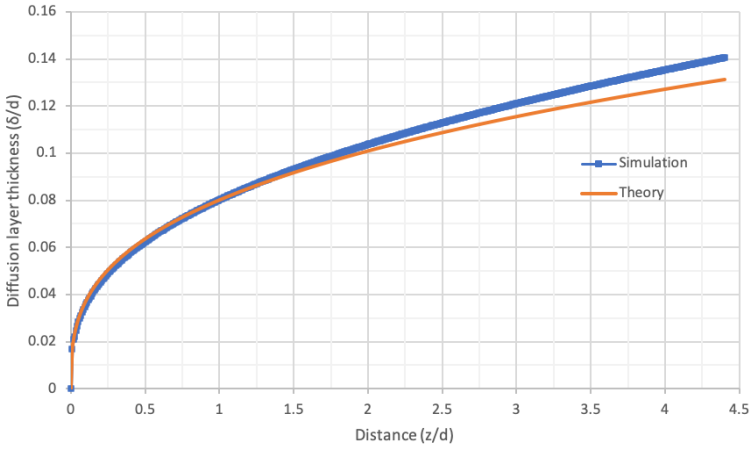

Figure 4.7: Comparison of Nernst diffusion layer thickness from simulation with theoretical value for a pipe-flow cell(δ_N). $E_A = -3.6V, u_{TP} = 0.04m.s^{-1}, d = 100\mu m$

The two curves agree reasonably well and thereby verifies that the model predictions are accurate and consistent enough to derive conclusions. With both the electroanalysis and hydrodynamics verified, the electrochemical model is successfully validated. Chapter 5 discusses the results and trends extracted from the model.

5

Results and Discussion

The current chapter investigates the performance of the flow cell using the electrochemical model developed in section 3.1. The model is solved in COMSOL Multiphysics to generate results that answer the research questions posed in section 1.3. section 5.1 discusses the performance of the Taylor-flow cell relative to the laminar-pipe-flow cell. Results from parametric studies are explained in section 5.2. section 5.3 examines the effect of bubble dissolution using the quasi-steady-state approach described in subsection 3.1.2. Finally, based on the insights from previous sections, a 1D mass transfer model is proposed in section 5.4.

Please note: Unless otherwise stated, the following parameters are used for all the simulations in this chapter: $u_B = 0.04m.s^{-1}, \epsilon_B = 0.5, d = 100\mu m, E_A = -3.6V$ (mass transfer limiting case) and $\epsilon_{FE} = 100\%$.

5.1. Performance Assessment

Polarisation curves The flow cell performance is assessed using current densities and polarisation curves (j-E). The average current density at the cathode, as shown in Figure 5.1 is calculated for different electrode potentials for flow cells with Taylor flow and pipe flow. The laminar-pipe-flow cell[1] is chosen as a reference, to quantify the effect of the Taylor flow on flow cell performance. Figure 5.1 clearly shows that the Taylor flow has increased the cell productivity with the limiting current density over 1000 $\frac{mA}{cm^2}$, an order of magnitude higher than the limiting current density observed in pipe flow. Simple calculation finds that the flow cell energy efficiency is 25% for achieving a current density of 300 $\frac{mA}{cm^2}$ (based on performance metrics). Even though Taylor flow can achieve high current densities, the efficiency of the cell still suffers from sluggish kinetics. Therefore, an electrochemical cat-

[1] Details regarding the simulation settings, boundary conditions for the laminar-pipe-flow cell can be found in Appendix B

alyst with a higher catalyst activity is recommended to take full advantage of the Taylor-flow cell.

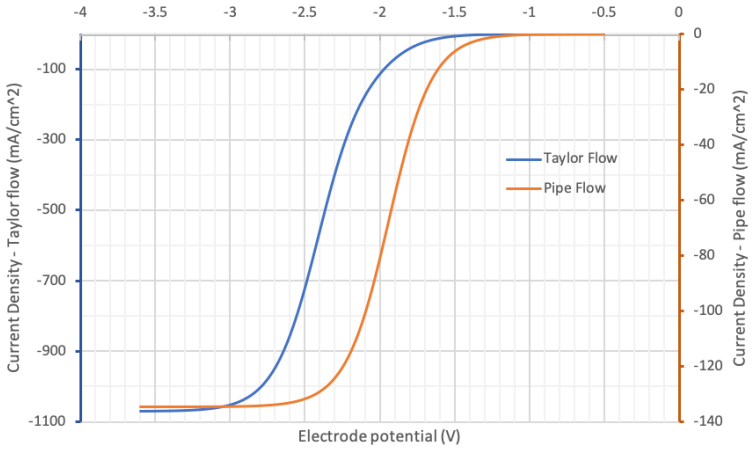

Figure 5.1: Polarisation curves for Taylor-flow cell and laminar-pipe-flow cell

In the following discussions, an effort has been made to elucidate the reasons behind the increased current densities.

Concentration and velocity profiles The velocity-magnitude distribution and concentration distribution are shown in Figure 5.2. In the liquid slug, the velocity-magnitude follows a parabolic velocity profile and the streamlines show the expected vortices. Vortices make liquid to circulate, which homogenises it. Notably from Figure 5.2, the concentration contours also follow the streamlines showing that the convection is the dominant process in the slug region. Concentration profile, as shown in Figure 4.4b, also depicts a uniform concentration in the region where vortices are present, and a linear profile is observed close to the cathode. Close to the cathode, diffusion influences the species transport in liquid slug and the film.

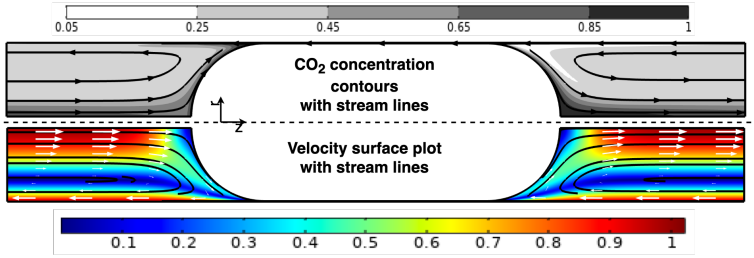

Figure 5.2: Surface plot with concentration contours, stream lines and velocity profiles, $E_A = -2.1V$
Note: The concentration and velocity magnitude are shown in non-dimensional units.

Diffusion Layer The diffusion rate at the cathode determines the limiting current density. Qualitatively, the diffusion rate is visualised using the concentration boundary layer or the diffusion layer. In general, as the diffusion layer gets thicker the diffusion rate decreases. Mathematically, the diffusion layer thickness is written as Equation 5.1.

$$\delta(x) = \frac{C_{bulk}(x)}{(-\partial c(x)/\partial n_x)} \tag{5.1}$$

where C_{bulk} is the bulk concentration, x is any position and n_x is normal at x. For Taylor flow, the bulk concentration is assumed to be the volumetric average concentration of CO_2 in the liquid phase. Using Equation 5.1, the diffusion layer thickness in Taylor flow is calculated along the cathode length and compared with the Nernst diffusion layer in pipe flow. The Nernst diffusion layer is determined from Equation 4.2. Figure 5.3 shows the outcome of the simulation for two different bubble velocities.

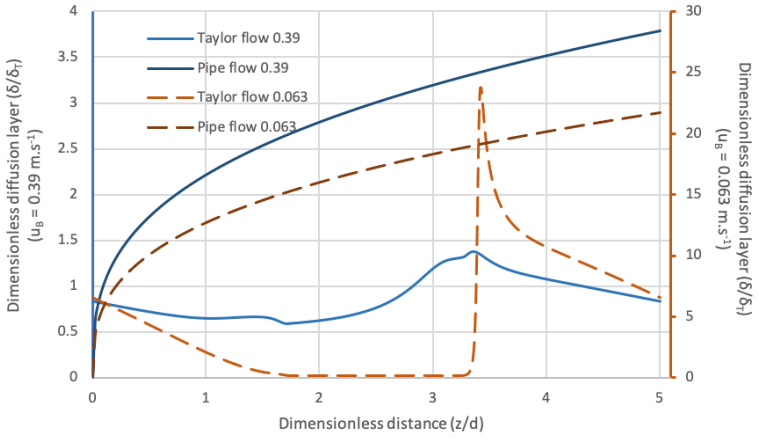

Figure 5.3: Comparison of diffusion layer thickness between Taylor flow and Pipe flow at two different bubble velocities. Note: The diffusion layer thickness (δ) is scaled with Taylor film thickness (δ_T).

A duck-shaped profile is observed for the calculated diffusion layers in the unit cell. An important observation is that for low velocities, diffusion layers in the slug region are much thicker than the film thickness and gets closer to film thickness at high velocity. The apparent reason is that at higher velocities, the re-circulation rate in liquid slugs increases, and as a consequence, the diffusion layer thickness decreases. Nevertheless, in both cases, the diffusion layer thickness for the Taylor flow is smaller than the pipe flow. As a result, the rate of diffusion or mass transfer rate for the Taylor flow is higher than the pipe flow ergo limiting current density which is illustrated in Figure 5.1.

5.2. Parametric Study

Effect of bubble velocity A parametric study with bubble velocity (u_B) is performed to analyse it's effect on cell performance. The cell performance is assessed by monitoring the limiting current density (j_{lim}) and the average diffusion layer thickness(δ_{av}). Figure 5.4 shows the outcome.

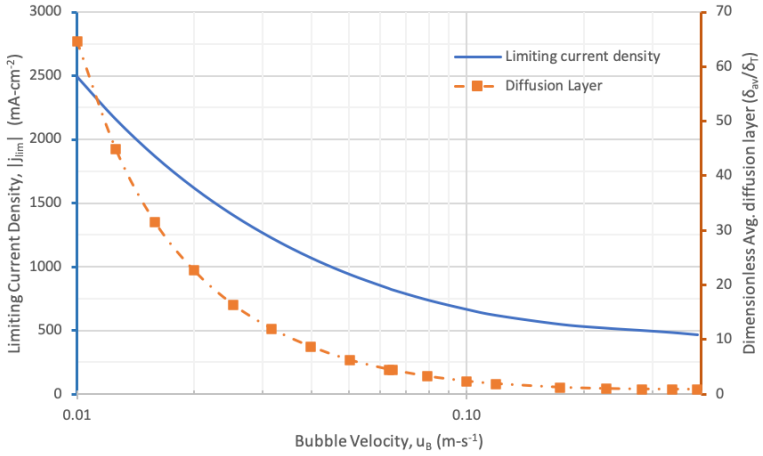

Figure 5.4: The effect of velocity on limiting current density and average diffusion layer.
Note: The diffusion layer thickness (δ) is scaled with Taylor film thickness (δ_T).Only absolute values of the current density are considered

Figure 5.4 uses a logarithmic scale on the x-axis for better resolution of variables at low velocities. Even though the diffusion layer is getting thinner with an increase in velocity, the model predicts a decrease in limiting current density. The reason becomes evident when individual contribution to the current density by film and slug regions is isolated. The Equation 5.2 calculates the contribution of slug region (S) to the overall current density ($|j_{lim}|$)

$$\%S = \frac{(1-\epsilon_B)|j^S_{lim}|}{|j_{lim}|} \times 100 \tag{5.2}$$

where $|j^S_{lim}|$ is the absolute value of average current density over the slug length. Figure 5.5 shows the outcome. At low velocities, the diffusion layer in the slug region is very thick, as shown in Figure 5.3 and 5.4. Therefore, the slug region has low mass transfer rate and accounts for the small contributions depicted in Figure 5.5. In the bubble or film region, the diffusion layer coincides with the film thickness (δ_T) and as the velocity decreases the film thickness becomes even smaller. The diffusion rate in the film region thus increases and justifies the increase in limiting current density observed at low velocities. At high velocities, where the diffusion layer in the slug region is of the same order as the film thickness, the contributions of both regions become equal, as shown in Figure 5.5. But the improvement observed in the slug region is relative; as the velocity increases the film also becomes

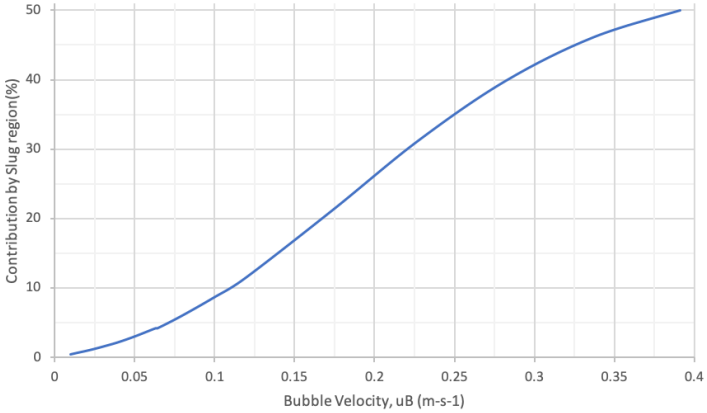

Figure 5.5: The effect of velocity on liquid slug contribution and current densities.

thicker. Hence the overall mass transfer rate still suffers - consequently, the limiting current density.

Effect of void fraction and diameter Based on the above discussion, it is clear that changes to the film region have a direct impact on cell performance. The results from the parametric study of void fraction and diameter further reinforce this concept. The limiting current density increases with the void fraction, and the apparent reason is that the contribution of film region to the current density has increased. The linear behaviour depicted in Figure 5.6 is expected at low velocities, where the current density in the slug region can be neglected. Therefore, the overall current density is proportional to the void fraction.

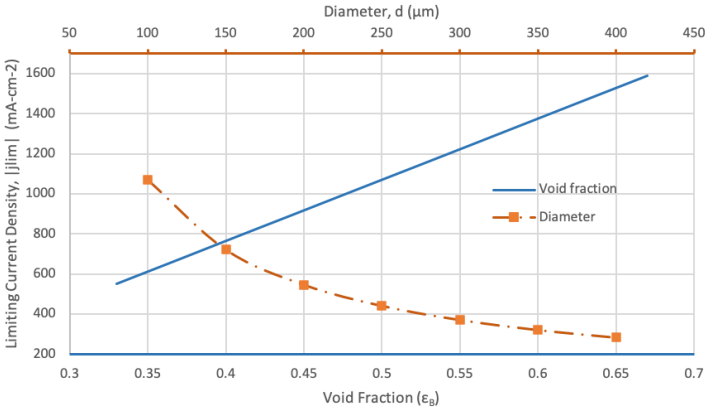

Figure 5.6: The effect of void fraction and diameter on limiting current density.
Note: Only absolute values of the current density are considered

Similarly, as the diameter increase, the film thickness also increases and thus reduced current densities are expected, as shown in Figure 5.6. Also, a linear decrease in current densities with the increase in diameter was anticipated according to the Equation 2.1. But the exponential nature at the beginning suggests that the slug region has a role in mass transfer at smaller diameters.

The parametric analysis shows that the film thickness plays a significant role in improving the productiveness of the flow cell, and the role of the slug region is limited to high velocities.

5.3. Bubble Dissolution

The studies so far discussed observations that are valid in the initial stage of the process where the changes in bubble size are negligible. Eventually, as the reaction continues, the bubble starts to dissolve and affects mass transport ergo cell performance, due to change in the interfacial area. This section discusses the effect of bubble dissolution on flow cell performance at different flow conditions. In addition to the limiting current density, the performance of the cell is monitored using interface-mass transfer coefficient $-k_L a$. The role of interface-mass transfer coefficient is identical to the diffusion layer, i.e. to qualitatively understand the mass transfer rates at the interface. Mathematically, $k_L a$ is related to the interface-mass transfer rate according to Equation 5.3.

$$(k_L a).(C^0_{CO_2} - \bar{C}) \times V_{uc} = \int_{A_I} (J_{I,CO_2}.n)dA \tag{5.3}$$

where V_{uc} is the unit cell volume and $\bar{C}$ is the volumetric average concentration defined as $\bar{C} = \frac{\int c.dV}{\int dV}$. Since $k_L a$ is proportional to interface-mass transfer, it also gives information on bubble dissolution rate. The bubble dissolution is modelled through quasi-steady-state analysis, as explained in subsection 3.1.2. Equation 3.12 is solved numerically in Matlab[2] to determine the bubble size at discrete time intervals. The author made two essential assumptions to determine the bubble shape: First, the bubble is assumed to shrink only in the axial direction. The assumption holds for low dissolution rates, where the interface movement is minimal. Since the slow-moving interface doesn't affect the hydrodynamics in the liquid slug, the film thickness can be assumed constant and consequently, forces the bubble to shrink only in the axial direction. The second assumption is that the volume of liquid slug remains constant. The simple justification is that the dissolution of CO_2 bubble adds a little volume to H_2O due to significant differences in densities between liquid and gas. The bubble size is quantified using a void fraction. The electrochemical model is then solved in each interval, i.e. for each bubble size to determine the $k_L a$ and the limiting current density and the results are shown in Figure 5.7 and Figure 5.8.

The interface-mass transfer coefficient, as shown in Figure 5.7, is observed to decrease as the bubble shrinks. The apparent reason is that the interfacial area for

[2] Appendix C has the Matlab code

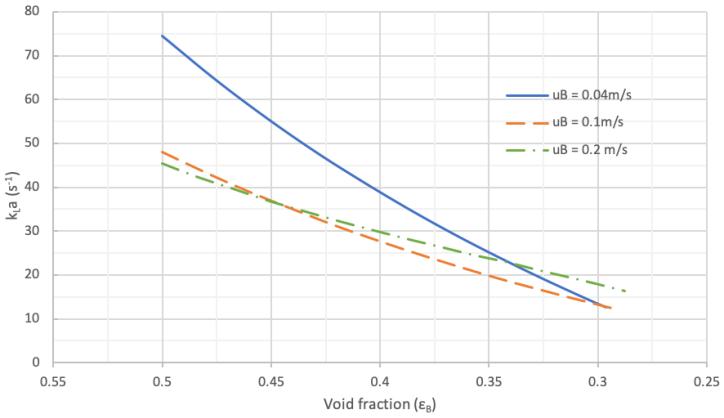

Figure 5.7: The effect of bubble dissolution on k_La for different bubble velocities

5

mass transfer as well as the unit cell volume is decreasing as the bubble diminishes. Notably, the rate at which k_La declines, increases at lower velocities, which is understandable because for low velocities films are thinner, leading to high mass transfer rates. Thus, initially, when the mass transfer rates are very high, the dissolution rates are also higher, and the bubble shrinks at a faster rate - subsequently the mass-transfer coefficient. Later, as the bubble shrinks Figure 5.7 describes the opposite behaviour. It shows that the value of k_La to be more significant for higher velocities. The possible reason is that as transport through film decreases, the contribution made by the slug area becomes relevant. As discussed in section 5.2, the transport in slug region is substantial at higher velocities. Therefore, the increase in k_La is a result of the increased transport of CO_2 through liquid slug.

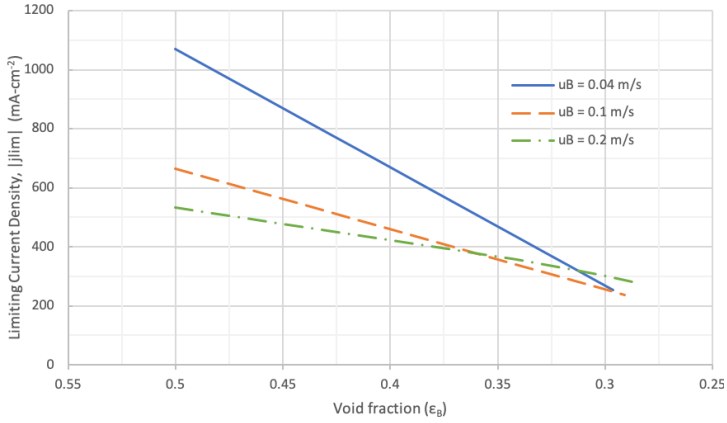

Figure 5.8: The effect of bubble dissolution on the current density for different bubble velocities
Note: Only absolute values of the current density are considered

Under steady-state, the mass transfer rate at the interface is equal to the mass transfer rate at the cathode given that the net-flux through inlet and outlet is zero. In the present work, the net-flux through inlet and outlet is made zero through the periodic boundary condition. Therefore, the trends observed for $k_L a$ and their reasoning should extend to the results for current density. Figure 5.8 shows the anticipated results for the limiting current density.

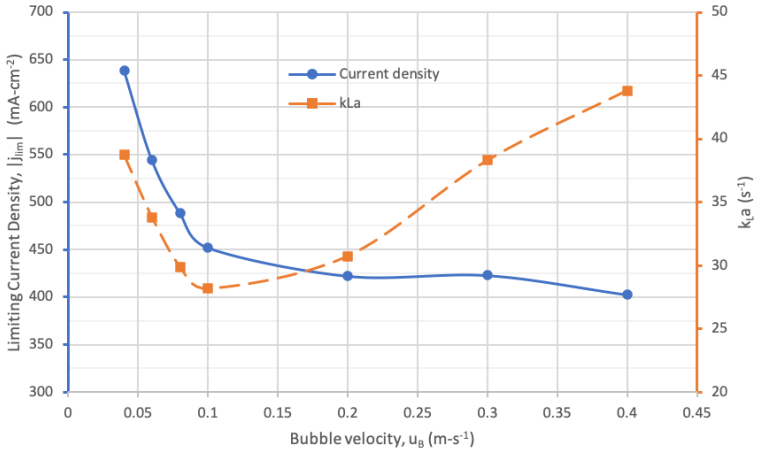

Figure 5.9: The effect of bubble velocity on avg. limiting current density and avg. $k_L a$.
Note: Only absolute values of the current density are considered

As the bubble diminishes, Figure 5.7 and 5.8 illustrates the change in $k_L a$ and limiting current density with time. Thus, to resolve the overall performance of the flow cell, the average limiting current density and $k_L a$ are determined, for different bubble velocities. Figure 5.9 shows the outcome. Notably, the interface-mass transfer coefficient has a minimum, and accordingly, two distinct regions can be identified:

Region I On the left side of minimum, thinner films improve the mass transfer rate and current densities in the film region. The contribution from the slug region is minimal, as explained in section 5.2. Therefore, any improvement in transport in the film region directly improves current densities ,i.e. cell performance. As the bubble dissolves, large variation in current density limits are observed in this region.

Region II On the right side of minimum, the mass transfer is improved due to increased circulation rate in the slug region, forming thinner diffusion layers close to the cathode and interface. The thicker films in the film region nullify the improvement in mass transfer in the slug area at the cathode. Therefore, a lower limiting current density is illustrated in Figure 5.9. Due to the competition between film and slug regions, the difference in the current density limits is low in this region.

5.4. 1D Model

The core idea behind this thesis is to assess the performance of a Taylor-flow cell and is done so by calculating current density at the electrode. From a pragmatic perspective, it is not always feasible to solve the 2D electrochemical model. Therefore, It is of interest to further simplify the model and get quick and accurate estimates of current densities. Accordingly, a 1D model is developed based on the insights from the results of the 2D electrochemical model. The summary of the 1D model equations[3] is given below:

$$\text{Total Current Density:} \quad j = \frac{Da(\eta)}{1+Da(\eta)} . j_{lim}, \tag{5.4}$$

$$\text{Limiting Current Density:} \quad j_{lim} = \frac{nFD}{\delta} . \frac{C^o_{CO_2} . A_f + \bar{C} A_s}{A_f + A_s} \tag{5.5}$$

$$\text{Average concentration:} \quad \bar{C} = \frac{k_L C^o_{CO_2}}{k_L + k'} \tag{5.6}$$

$$\text{Bubble dissolution rate:} \quad -C_b \frac{\partial V_b}{\partial t} = \frac{j}{nF} \times (A_f + A_s) \tag{5.7}$$

where, $Da(\eta) = \frac{k(\eta)\delta}{D}$ is Damkohler number, k_L is the mass transfer coefficient obtained from correlation derived from the penetration theory and stated as $k_L = 2\sqrt{\frac{2Du_B}{\pi^2 d}}$[27, 31, 41]. $k' = \frac{D}{\delta} \times \frac{Da(\eta)}{1+Da(\eta)} \times \left(1 + \frac{L_S}{d_b}\right)$ and $k(\eta)$ is defined using Butler-Volmer kinetics[25] given by Equation 3.11. The above equations are solved using Matlab[4] and results are compared with the 2D model for validation. Figure 5.10 shows the polarisation curve and illustrates that 1D model matches reasonably well with the 2D model with a maximum estimated error of 5%.

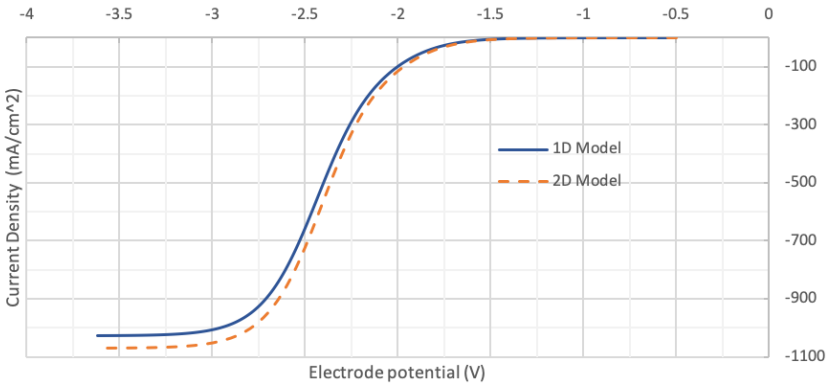

Figure 5.10: Validation of 1D model by comparing the results with 2D model

[3] Appendix E has detailed derivation of the 1D model
[4] Appendix C has the matlab code.

Similar results were predicted for the dissolution of the bubble, as shown in Figure 5.11. Notably, the error in the limiting current density is persistent throughout the dissolution of the bubble. The errors suggest that either the correlation for mass transfer coefficient (k_L) or the assumption made for diffusion layer thickness lead to the observed deviation. For better understanding, the mass transfer coefficient is first verified with the simulation for different bubble velocities. Figure 5.12 shows the outcome.

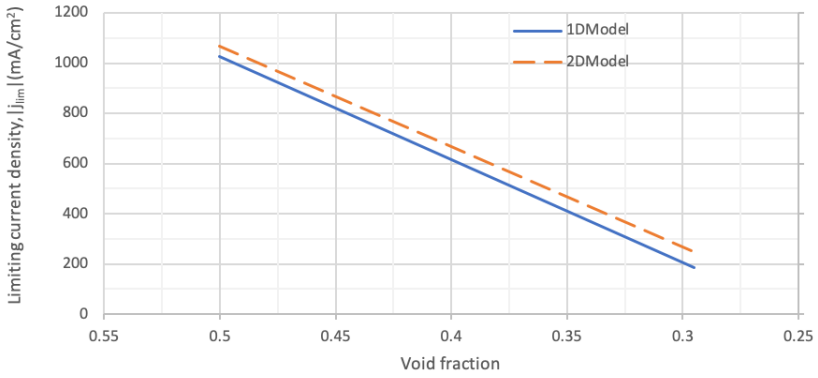

Figure 5.11: The effect of dissolution on Limiting current density - 1D Model.

The mass transfer coefficient from correlation, as shown in Figure 5.12 is under-estimating the values obtained from the 2D model. Consequently, the current densities depicted in Figure 5.10 and Figure 5.11 are also under-estimated by the 1D model.

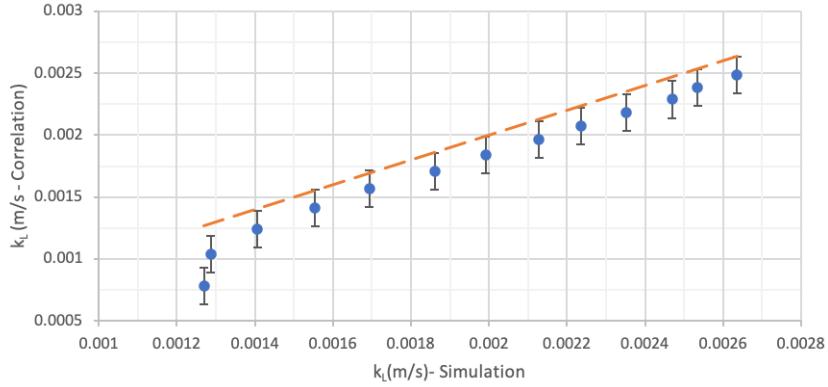

Figure 5.12: Verification of k_L correlation at bubble caps. Error bars represent standard error

A parametric study of limiting current density with velocity is shown in Figure 5.13 and illustrates that the limiting current density values start deviating at high veloci-

ties. The maximum estimated error at high velocities is 11% and is higher than the error from mass transfer correlation. The apparent reason is that the assumption for the diffusion layer thickness creates the observed deviation.

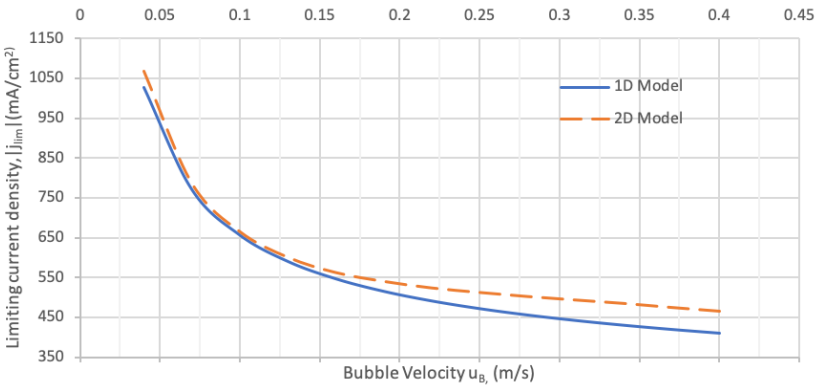

Figure 5.13: The effect of bubble velocity on Limiting current density - 1D model

The results from the 1D model agree reasonably well with the 2D model, especially at low velocities, and therefore can be used for simple estimates for calculating current densities at different process conditions.

6

Conclusion

Taylor flow in an electrochemical flow cell is an innovative concept proposed to improve the performance of the flow cell; ergo a numerical investigation is carried out to verify the hypothesis. The current study implements a modelling approach which integrates the frequently-used unit cell strategy for Taylor flow with electrochemistry. Theoretical concepts and experimental work by Thulasidas et al. [39], Abiev [52] are used to verify and validate the model. Results from the model are analysed to assess the performance of the Taylor-flow cell. This section discusses key insights from the analysis.

The results show a significant improvement in the performance, i.e. in the current densities, of the Taylor-flow compared to a typical flow (pipe-flow) cell. The maximum calculated current densities increase by an order of magnitude under certain flow conditions. Despite reporting high limiting-current densities, the energy efficiency of the flow cell is found lower than the values recommended from the techno-economic analysis[9], owing to sluggish kinetics. A catalyst with high activity is recommended to improve efficiency. The bulk of the liquid phase has uniform concentration, because of vortices, except near the caps and cathode. At the cathode surface, a duck-shaped diffusion layer profile is observed along the unit cell length. The thickness of the diffusion layer in the film region is the same as the Taylor-film thickness. In the liquid-slug area, the diffusion layer thickness is dependent on the velocity.

Parametric studies with bubble velocity reveal opposite trends for the diffusion layer in film and slug region. In the film region, the diffusion layer thickness increases with the speed while in the slug region, it decreases. The investigation of the individual contribution of the film and slug region reveals that the film contribution is more significant than the slug region. Subsequently, the overall limiting-current density drops monotonically with the velocity, within the established range.

Examining the devolution of the bubble shows that the current densities deteriorate as the bubble dissolves because of the electrochemical reaction—consequently, a range of current densities specific to a flow condition are observed. At slowest speeds, the difference in the current density-limits increases. As the current densities change between the extremes, the stability of the cell gets affected. On the contrary, at highest speeds, the competition between slug and film region reduces the gap between the current density-limits, showing better stability but comes at the expense of lower current densities. Therefore, an optimum velocity can be determined to balance the current density and stability. Nevertheless, the average current densities observed in the Taylor-flow cell with bubble dissolution are still higher than the pipe-flow cell, indicating an overall improvement in its performance.

Conclusively, a 1D model is developed, based on the insights from the 2D electrochemical model, to determine the current densities and dissolution rates. The model agrees reasonably well with the 2D electrochemical model, especially at low velocities. The author recommends the use of the 1D model for the practical estimation of current densities in the range described in Table 4.1. Error analysis shows that by improving the correlation for mass transfer coefficient at caps or for the diffusion layer thickness at the cathode enhances the model accuracy.

6.1. Future Opportunities

The first assessment of Taylor flow on electrolysis shows promising results. There is a need for improvement in the model and following recommendations are made:

- **Experimental studies for kinetics** The kinetic parameters for the electrochemical reaction are system-specific. It is recommended to conduct some experiments with Taylor-flow cell and verify the kinetics used in this Thesis.
- **Dimensionless analysis** It is recommended to perform an order of magnitude analysis to further the understanding of the system and generalise the concepts that are discussed in this Thesis.
- **Homogeneous reactions** The model ignored the dissociation of CO_2 in water. A homogeneous reaction reduces the availability of CO_2 and effects the current density at the cathode. Hence, it is recommended to implement the homogeneous reaction to get more realistic current densities.
- **Bubble shape** The current work assumes the shape of the bubble to be an elongated sphere by neglecting the inertial forces. The assumption can be relaxed to increase the range of operating conditions for the model. The shape of the bubble can be considered by incorporating surface tension effects at the interface using the Young–Laplace equation.
- **Extending the model** The information from current model is restricted to the half-cell reaction at the cathode. It can be extended to implement ion-transport through membrane and reaction at the anode.

References

[1] D. T. Whipple and P. J. Kenis, *Prospects of CO2 utilization via direct heterogeneous electrochemical reduction,* Journal of Physical Chemistry Letters **1**, 3451 (2010).

[2] *Supplementary Figure 1: PXRD patterns of Ag-Al precursors, as-prepared np-Ag electrodes and np-Ag electrodes after 2 hours electrolysis under -0.5 V vs. RHE.* , 1.

[3] T. Kuramochi, A. Ramírez, W. Turkenburg, and A. Faaij, *Comparative assessment of CO 2 capture technologies for carbon-intensive industrial processes,* Progress in Energy and Combustion Science **38**, 87 (2012).

[4] International Energy Agency, World Energy Outlook., Tech. Rep. 2 (2017).

[5] *e-Refinery,* .

[6] O. S. Bushuyev, P. De Luna, C. T. Dinh, L. Tao, G. Saur, J. van de Lagemaat, S. O. Kelley, and E. H. Sargent, *What Should We Make with CO2 and How Can We Make It?* (2018).

[7] D. R. Kauffman, J. Thakkar, R. Siva, C. Matranga, P. R. Ohodnicki, C. Zeng, and R. Jin, *Efficient Electrochemical CO<inf>2</inf> Conversion Powered by Renewable Energy,* ACS Applied Materials and Interfaces **7**, 15626 (2015).

[8] S. Verma, B. Kim, H. R. M. Jhong, S. Ma, and P. J. Kenis, *A gross-margin model for defining technoeconomic benchmarks in the electroreduction of CO2,* ChemSusChem **9**, 1972 (2016).

[9] M. G. Kibria, J. P. Edwards, C. M. Gabardo, C. T. Dinh, A. Seifitokaldani, D. Sinton, and E. H. Sargent, *Electrochemical CO2 Reduction into Chemical Feedstocks: From Mechanistic Electrocatalysis Models to System Design,* Advanced Materials **31**, 1 (2019).

[10] S. Hernández, M. Amin Farkhondehfal, F. Sastre, M. Makkee, G. Saracco, and N. Russo, *Syngas production from electrochemical reduction of CO 2 : current status and prospective implementation,* Green Chemistry **19**, 2326 (2017).

[11] B. Kim, S. Ma, H. R. Molly Jhong, and P. J. Kenis, *Influence of dilute feed and pH on electrochemical reduction of CO2 to CO on Ag in a continuous flow electrolyzer,* Electrochimica Acta **166**, 271 (2015).

[12] T. Burdyny and W. A. Smith, *CO2 reduction on gas-diffusion electrodes and why catalytic performance must be assessed at commercially-relevant conditions,* Energy and Environmental Science **12**, 1442 (2019).

[13] D. T. Whipple, E. S.-s. Lett, D. T. Whipple, E. C. Finke, and P. J. A. Kenis, *Letters Microfluidic Reactor for the Electrochemical Reduction of Carbon Dioxide : The Effect of pH Microfluidic Reactor for the Electrochemical Reduction of Carbon Dioxide : The Effect of pH,* , 109 (2010).

[14] S. Hernández, M. Amin Farkhondehfal, F. Sastre, M. Makkee, G. Saracco, and N. Russo, *Supporting information (si) syngas production from electrochemical reduction of co2,* (2017).

[15] Y. Hori, H. Ito, K. Okano, K. Nagasu, and S. Sato, *Silver-coated ion exchange membrane electrode applied to electrochemical reduction of carbon dioxide,* Electrochimica Acta **48**, 2651 (2003).

[16] Y. Hori, H. Wakebe, T. Tsukamoto, and O. Koga, *Electrocatalytic process of CO selectivity in electrochemical reduction of CO2 at metal electrodes in aqueous media,* Electrochimica Acta **39**, 1833 (1994).

[17] J. Durst, A. Rudnev, A. Dutta, Y. Fu, J. Herranz, V. Kaliginedi, A. Kuzume, A. A. Permyakova, Y. Paratcha, P. Broekmann, and T. J. Schmidt, *Electrochemical CO2 reduction -A critical view on fundamentals, materials and applications,* Chimia **69**, 769 (2015).

[18] H.-R. M. Jhong, F. R. Brushett, and P. J. A. Kenis, *The effects of catalyst layer deposition methodology on electrode performance,* Advanced Energy Materials **3**, 589 (2013).

[19] Q. Lu, J. Rosen, Y. Zhou, G. S. Hutchings, Y. C. Kimmel, J. G. Chen, and F. Jiao, *A selective and efficient electrocatalyst for carbon dioxide reduction,* Nature Communications **5**, 1 (2014).

[20] H.-r. M. Jhong, S. Ma, and P. J. A. Kenis, *Electrochemical conversion of CO2 to useful chemicals: status , remaining challenges , and future opportunities,* , 191 (2013).

[21] B. A. Rosen, A. Salehi-khojin, M. R. Thorson, W. Zhu, D. T. Whipple, P. J. A. Kenis, and R. I. Masel, *Ionic Liquid – Mediated Selective Conversion of CO 2 to CO at low overpotentials,* Science , 643 (2011).

[22] S. Messias, M. M. Sousa, M. Nunes da Ponte, C. M. Rangel, T. Pardal, and A. S. Reis Machado, *Electrochemical production of syngas from CO 2 at pressures up to 30 bar in electrolytes containing ionic liquid ,* Reaction Chemistry & Engineering , 1982 (2019).

[23] M. Alvarez-Guerra, J. Albo, E. Alvarez-Guerra, and A. Irabien, *Ionic liquids in the electrochemical valorisation of CO2,* Energy and Environmental Science **8**, 2574 (2015).

[24] A. S. S. Bhargava, F. Proietto, D. Azmoodeh, E. R. Cofell, D. A. Henckel, S. Verma, C. J. Brooks, A. A. Gewirth, and P. Kenis, *System Design Rules for Intensifying the Electrochemical Reduction of CO2 to CO on Ag Nanoparticles,* ChemElectroChem , accepted article (2020).

[25] A. J. Bard, L. R. Faulkner, J. Leddy, and C. G. Zoski, Electrochemical methods: fundamentals and applications, Vol. 2 (wiley New York, 1980).

[26] R. K. Edvinsson and S. Irandoust, *Finite-Element Analysis of Taylor Flow,* AIChE Journal **42**, 1815 (1996).

[27] M. T. Kreutzer, F. Kapteijn, J. A. Moulijn, and J. J. Heiszwolf, *Multiphase monolith reactors: Chemical reaction engineering of segmented flow in microchannels,* Chemical Engineering Science **60**, 5895 (2005).

[28] M. T. Kreutzer, F. Kapteijn, J. A. Moulijn, C. R. Kleijn, and J. J. Heiszwolf, *Inertial and interfacial effects on pressure drop of Taylor flow in capillaries,* AIChE Journal **51**, 2428 (2005).

[29] N. Shao, W. Salman, A. Gavriilidis, and P. Angeli, *CFD simulations of the effect of inlet conditions on Taylor flow formation,* International Journal of Heat and Fluid Flow **29**, 1603 (2008).

[30] R. Gupta, D. Fletcher, and B. Haynes, *Taylor flow in microchannels: A review of experimental and computational work,* Journal of Computational Multiphase Flows **2**, 1 (2010).

[31] N. Shao, A. Gavriilidis, and P. Angeli, *Mass transfer during Taylor flow in microchannels with and without chemical reaction,* Chemical Engineering Journal **160**, 873 (2010).

[32] T. Abadie, J. Aubin, D. Legendre, and C. Xuereb, *Hydrodynamics of gas-liquid Taylor flow in rectangular microchannels,* Microfluidics and Nanofluidics **12**, 355 (2012).

[33] J. M. Van Baten and R. Krishna, *CFD simulations of wall mass transfer for Taylor flow in circular capillaries,* Chemical Engineering Science **60**, 1117 (2005).

[34] F. L. D. Martínez and A. M. Billet, *Hydrodynamics And Mass Transfer In Taylor Flow,* , 1 (2015).

[35] V. Van Steijn, Formation and Transport of Bubbles in Microfluidic Systems, Ph.D. thesis (2010).

[36] F. P. Bretherton, *The motion of long bubbles in tubes,* Journal of Fluid Mechanics **10**, 166 (1961).

[37] P. Aussillous and D. Quere, *Quick deposition of a fluid on the wall of a tube,* Physics of Fluids **12**, 2367 (2000).

[38] J. A. Howard and P. A. Walsh, *Review and extensions to film thickness and relative bubble drift velocity prediction methods in laminar Taylor or slug flows,* International Journal of Multiphase Flow **55**, 32 (2013).

[39] T. C. Thulasidas, M. A. Abraham, and R. L. Cerro, *Flow patterns in liquid slugs during bubble-train flow inside capillaries,* Chemical Engineering Science **52**, 2947 (1997).

[40] T. C. Thulasidas, M. A. Abraham, and R. L. Cerro, *Bubble-train flow in capillaries of circular and square cross section,* Chemical Engineering Science **50**, 183 (1995).

[41] J. M. van Baten and R. Krishna, *CFD simulations of mass transfer from Taylor bubbles rising in circular capillaries,* Chemical Engineering Science **59**, 2535 (2004).

[42] A. West, Electrochemistry and Electrochemical Engineering: An Introduction (Alan C. West, 2012).

[43] N. V. Gadgil, *Modeling a Flow-Cell for Electrochemical Reduction of Carbon Dioxide to Formate,* , 77 (2018).

[44] S. C. Chapra, R. P. Canale, et al., Numerical methods for engineers (Boston: McGraw-Hill Higher Education„ 2010).

[45] K. Wu, E. Birgersson, B. Kim, P. J. Kenis, and I. A. Karimi, *Modeling and experimental validation of electrochemical reduction of CO2 to CO in a microfluidic cell,* Journal of the Electrochemical Society **162**, F23 (2015).

[46] G. Yu, B. Yu, S. Sun, and W. Q. Tao, *Comparative study on triangular and quadrilateral meshes by a finite-volume method with a central difference scheme,* Numerical Heat Transfer, Part B: Fundamentals **62**, 243 (2012).

[47] R. Gupta, D. F. Fletcher, and B. S. Haynes, *On the CFD modelling of Taylor flow in microchannels,* Chemical Engineering Science **64**, 2941 (2009).

[48] D. F. Fletcher and B. S. Haynes, *CFD simulation of Taylor flow: Should the liquid film be captured or not?* Chemical Engineering Science **167**, 334 (2017).

[49] F. L. Durán Martínez, C. Julcour, A. M. Billet, and F. Larachi, *Modelling and simulations of a monolith reactor for three-phase hydrogenation reactions — Rules and recommendations for mass transfer analysis,* Catalysis Today **273**, 121 (2016).

[50] W. Frei, *Solutions to linear systems of equations: Direct and iterative solvers,* COMSOL Multiphysics .

[51] G. I. Taylor, *Deposition of a viscous fluid on a plane surface,* Journal of Fluid Mechanics **9**, 218 (1960).

[52] R. S. Abiev, *Simulation of the slug flow of a gas-liquid system in capillaries,* Theoretical Foundations of Chemical Engineering **42**, 105 (2008).

[53] J. Yue, G. Chen, Q. Yuan, L. Luo, and Y. Gonthier, *Hydrodynamics and mass transfer characteristics in gas-liquid flow through a rectangular microchannel,* Chemical Engineering Science **62**, 2096 (2007).

[54] v. L. Graetz, *Ueber die wärmeleitungsfähigkeit von flüssigkeiten,* Annalen der Physik **254**, 79 (1882).

A

List of assumptions

Table A.1: An extensive list of assumptions made for the electrochemical model

No.	Assumption
A-1	Process is Isothermal
A-2	Gases and liquids show ideal behaviour
A-3	Instantaneous transfer of OH^- ions through membrane
A-4	Electrochemical catalyst is uniformly coated around the microchannel
A-5	Inertial and gravitational forces are negligible
A-6	Shape of the bubble caps is assumed to be hemispherical
A-7	Length of unit cell and void fraction can be varied independently
A-8	Stagnant Filme assumption: The film is assumed to be stationary.
A-9	Incompressible and Newtonian fluid
A-10	Fully developed flow is considered
A-11	Dilute solution
A-12	At the interface instant equilibrium is assumed
A-13	No migration inside the channel
A-14	Faraday's law is valid
A-15	Electric double layer is ignored
A-16	100% Faradic efficiency
A-17	Mass transfer resistance inside the catalyst is negligible
A-18	Homogeneous reactions are absent
A-19	Periodic boundary condition is applicable to the Mass transfer
A-20	Quasi-steady-state analysis is valid
A-21	The electrochemical reaction rate follows butler-volmer kinetics

B

Pipe-Flow cell

In this chapter simulation settings for the pipe-flow cell, used for comparative studies, are discussed.

B.1. Mesh

A quadrilateral mesh is generated as shown in **??**. Close to boundaries elements with high aspect ratio are made to capture the boundary layer.

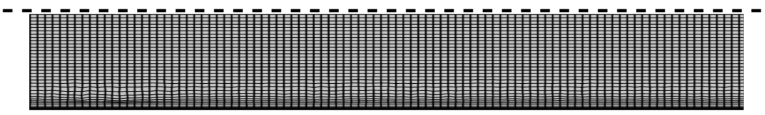

Figure B.1: Mesh for Pipe-Flow cell

B.2. Boundary conditions

For the velocity, fully-developed flow profile with average velocity equal to the liquid phase velocity of Taylor flow is given as input. And at outlet pressure is made equal to zero.

For the concentration, the boundary conditions at the wall and axis remain same as that of Taylor flow. For Inlet boundary condition, saturated concentration of species, c_i^o is used. At the Outlet boundary condition, diffusive flux is made zero.

C

Matlab Code

Matlab has been used to solve for analytical models and to integrate parametric studies in COMSOL. This chapter provides all the key scripts used in this Thesis.

C.1. Abiev's Film profile

```
function [r,uF] = filmProfile(uB,d)
    mu1 = 0.00089;%Water viscosity (Pa-s)
    rho1 = 1000;%Water density (kg/m3)
    mu2 = 1.8e-5;%Air viscosity (Pa-s)
    rho2 = 1.275;%Air density (Kg/m3)
    sigma = 0.072;%Surface tension (N/m)
    Ca = mu1*uB/sigma; %Capillary Number
    delta = 0.67*Ca^(2/3)/(1+3.33*Ca^(2/3))*d;%Film thickness from ...
        correltation
    R = d/2; Rb = R-delta; %Determining radius of bubble and channel
    A = pi*R^2; Ab = pi*Rb^2; Af = A - Ab; %Determining area of ...
        channel, bubble and film
    uTP = uB;%Initial guess
    e = 0;v1 = mu1/rho1;v2=mu2/rho2;g=0;%Gravity is ignored
    qS = uTP*A;%Flow rate inside the slug
    qB = (uB*Ab);%Flow rate of bubble
    while(e==0)
        G1 = pi/8*((R^4-Rb^4)/mu1+Rb^4/mu2);
        G2 = pi/8*((R^4-Rb^4)/v1+Rb^4/v2);
        G3 = pi/4*(rho1-rho2)/mu1*Rb^2*(R^2-Rb^2);
        dpdx = ((G2-G3)*g-qS)/G1;%Calculating the pressure drop
        g1 = g - 1/rho1*dpdx; g2 = g - 1/rho2*dpdx;
        E1 = g1/4/v1; C1 = (rho1-rho2)*g*Rb^2/2/mu1;E2 = g2/4/v2;
        qF = (pi*R^2*(E1*R^2/2 - C1/2)-pi*Rb^2*(E1*(R^2-Rb^2/2) - ...
            C1*(log(R/Rb)+1/2))); %Calculating flow rate in film
        qb = (pi*Rb^2*(E1*(R^2-Rb^2) - ...
            C1*log(R/Rb)+E2*Rb^2/2));%Calculating flow rate in bubble
        s = 2*(abs(qS-qB)-abs(qF))/(abs(qS-qB)+abs(qF)); %Exit ...
            condition for the loop
```

```
25          qS = qB+qF;%Calculating flow rate in Slug
26          a = 1;
27          if(s<1e-7) %Tolerence
28              e = 1;
29          end
30      end
31      uTP = (qS/A)1 %The liquid-phase velocity calculated as output
32      r = linspace(Rb,R,40);
33      uF = ((E1*(R^2-r.^2)+C1*log(r./R))); %Calculating the film profile
34      uF = (uF-uB); %Calculating the film profile in reference frame
35      r = (r-Rb)/delta; %Scaling the film beteween 0 and 1
36      plot(r,uF); %Plotting the film profile
37  end
```

C.2. Bubble Dissolution

```
1   function [t, cAvg, eB, kLa, CD] = shrinkageModel(model)
2   % ---------- Initialisation --------%
3    I = Inputs(model); %getting inputs from comsol for the ...
         electrochemical model
4    dz = strcat(num2str(0),'[m]'); %initialisation
5    uB = strcat(num2str(0.3),'[m/s]'); %giving inputs
6    model.param.set('dz',dz); %Amount of lenght bubble shrinks
7    model.param.set('uB',uB);
8    model.hist.disable;
9    model.sol('sol1').run; %Running the model at time t = 0; model is ...
         solved for steady-state in comsol
10  % ------------------------------------------------------------------
11  %  modelName = fullfile('/Users/raizel/Desktop/Mass Transfer ...
        Shrink/ShrinkageFiles',['shrink' num2str(1)]);
12  %  mphsave(model,modelName); %Optional to save file for each run
13  % ------------------------------------------------------------------
14  %Initialising parameters and variables for next step
15  i = 1; cAvg(1) = mphglobal(model,'cAvg'); eB(1) = 0.5; tP  = ...
        4*I.delta^2/I.D;  t(1) = tP; dz = 0;
16  kLa(i) = mphglobal(model,'kLa');CD(i)   = mphglobal(model,'CD'); b = 0;
17
18  % ----------Shrinkage starts --------%
19    while(min(eB) >= 0.3 && b == 0)
20      i = i+1;
21      nuInt   = mphglobal(model,'Jint');%Mass Transfer rate at the ...
            interface calculated in comsol
22      dz    = dz + nuInt/(I.cB*pi*I.Rb^2)*tP;%Calculating the shrinkage ...
            amount
23      dz_dim= dz/I.d%non-dimensionalising for COMSOL
24      dz_S = strcat(num2str(dz_dim),'[m]'); %Decrease in size
25      model.param.set('dz',dz_S);
26      model.hist.disable;
27      model.sol('sol1').run; %Run for the new domain
28      cAvg(i) = mphglobal(model,'cAvg'); %Monitoring a list of ...
            parameters over time
29      kLa(i) = mphglobal(model,'kLa');
30      CD(i)   = mphglobal(model,'CD');
31      eB(i)  = mphglobal(model,'eB');
```

```
32      t(i)     = i*tP;
33      m = mphglobal(model, 'Luc_D')
34      v = mphglobal(model,'eB')
35      diff = abs(eB(i) - eB(i-1))/eB(i) %Condition for exiting loop if ...
            void fraction becomes constant
36      if diff <=1e-5 %Tolarence
37         b = 1;
38      end
39  %     modelName = fullfile('/Users/raizel/Desktop/Mass Transfer ...
        Shrink/ShrinkageFiles',['shrink' num2str(i)]);
40  %     mphsave(model,modelName);
41    end
42  % -----------Shrinkage Ends ---------%
43
44  end
45
46  function I = Inputs(model)
47      I = struct;
48      I.D = mphevaluate(model, 'DCO2');
49      I.c0 = mphevaluate(model, 'c0');
50      I.d  = mphevaluate(model, 'd');
51      I.L = 5*I.d;
52      I.e = mphevaluate(model, 'e');
53      I.uB  = mphevaluate(model, 'uB');
54      I.cB  = mphevaluate(model, 'cB');
55      I.Rb  = mphevaluate(model, 'db')/2;
56      I.Lb  = mphevaluate(model, 'Lb');
57      I.Luc  = mphevaluate(model, 'Luc');
58      I.delta = mphevaluate(model, 'delta');
59  end
```

C.3. 1D Model

```
1   function [e,jLim] = Model1D
2   uB = 0.04; %Velocity as input
3   E  = -3.1; %Overpotential
4   i = 1; b = 0;k = 1;%indices
5   [dz,e(k),jLim(k)] = dissolution(0); %initalisation
6   %-------------------------------------------------
7             %---Polarisation curves------%
8   %-------------------------------------------------
9   % E = linspace(-3.1:-0.05:-0.5);
10  for i = 1:length(E)
11
12      j(i) = jE(E(i),uB)/10;%Current density in mA/cm2
13
14  end
15  %-------------------------------------------------
16  %-------------------------------------------------
17            %---Bubble dissolution------%
18  %-------------------------------------------------
19  while (min(e)>=0.3 && b == 0)
20      k = k+1;
21      [dzN,e(k),jLim(k)] = dissolution(dz);
```

C

```
22      if (abs(e(k)-e(k-1))/e(k) < 1e-12)
23          b = 1;
24      end
25      dz = dz + dzN;
26  end
27  %-------------------------------------------------
28  plot(e,jLim/10); %Plotting
29
30  end
31  function j = jE(eta,uB)
32  %Parameters from 1D model.
33  n = 2; F = 96500; D = 1.9e-9; mu = 8.9e-4; sigma = 0.072; R = 8.314; ...
        T = 293;
34  CaB = mu*uB/sigma; d = 1e-4; delta = ...
        d*(0.66*CaB^(2/3)/(1+3.33*CaB^(2/3)));
35  Lb = 2.5*d; Ls = 2.5*d; db = d - 2*delta; Af = pi*d*(Lb-db); As = ...
        pi*d*(Ls+db);
36  c0 = 34; cRef = 40.9; kL = 2*sqrt(2*D*uB/pi^2/d); jEx = 0.091; alpha ...
        = 0.17;
37  k = jEx/n/F/cRef*exp(-alpha*F*eta/R/T); Da = k*delta/D; k1 = ...
        D/delta*Da/(1+Da)*(1+Ls/db);
38  %-------------------------------------------------
39  %1D Model equations for current density
40  cAvg = kL*c0/(kL+k1);
41  jLim = n*F*D/delta*(c0*Af+cAvg*As)/(Af+As);
42  j    = -Da/(1+Da)*jLim;
43
44  end
45
46  function [dzN,eB,jLim] = dissolution(dz)
47  %Parameters from 1D model.
48  n = 2; F = 96500; D = 1.9e-9; mu = 8.9e-4; sigma = 0.072; R = 8.314; ...
        T = 293;uB = 0.04; eta = -3.1;
49  CaB = mu*uB/sigma; d = 1e-4; delta = ...
        d*(0.66*CaB^(2/3)/(1+3.33*CaB^(2/3)));
50  Lb = 2.5*d-dz; Ls = 2.5*d; db = d - 2*delta; Af = pi*d*(Lb-db); As = ...
        pi*d*(Ls+db);
51  c0 = 34; cRef = 40.9; kL = 2*sqrt(2*D*uB/pi^2/d); jEx = 0.091; alpha ...
        = 0.17;
52  k = jEx/n/F/cRef*exp(-alpha*F*eta/R/T); Da = k*delta/D; k1 = ...
        D/delta*Da/(1+Da)*(1+Ls/db);
53  dt = 10*delta^2/D;
54  %1D Model equations for bubble dissolution rate
55  cAvg = kL*c0/(kL+k1);
56  jLim = n*F*D/delta*(c0*Af+cAvg*As)/(Af+As);
57  j    = Da/(1+Da)*jLim;
58  dzN   = j/n/F/(pi*db^2/4)/cRef*dt*(Af+As);
59  eB    = Lb/(Ls+Lb);
60  end
```

D

Dimensionless Equations

In COMSOL Multiphysics® the equations are implemented in dimensionless form and the summary of equations including boundary conditions for the electrochemical model are given below:

$$\text{Continuity:} \quad \nabla^*.u^* = 0 \tag{D.1}$$

$$\text{Navier-Stokes :} \quad Re(u^*.\nabla^* u^*) = -\nabla^* P^* + \nabla^{*^2} u^* \tag{D.2}$$

$$\text{Species Transport :} \quad Pe(u^*.\nabla^* c^*) = \nabla^{*^2} c^* \tag{D.3}$$

Table D.1: Boundary conditions for 2D Model - Dimensionless form

Boundary	Hydrodynamics	Species Transport
Inlet	$u^* = 2\left(1 - 4r^{*^2}\right) - \Psi\hat{z} + 0\hat{r}$	Periodic Boundary Condition
Outlet	$u^* = 2\left(1 - 4r^{*^2}\right) - \Psi\hat{z} + 0\hat{r}$, $P^* = 0$	Periodic Boundary Condition
Interface	Slip condition, $\frac{\partial u^*}{\partial n^*} = 0$ - Free surface	$c_i^* = \frac{c_i^o}{c_{CO_2}^o}$
Wall	No slip, $u^* = -\Psi\hat{z} + 0\hat{r}$	$-\nabla_n^* c_i^* = -\frac{R_{i,s}(\eta)}{D_{CO_2} c_{CO_2}^o / d}$

Note, the above equations are obtained by scaling all length's with diameter (d), all velocities or speeds with liquid-phase velocity (u_{TP}) and all concentrations with Saturated concentration of CO_2. Scaling of few variables are shown below:

$r = d.r^*$ $\qquad$ $z = d.z^*$

$\Psi = \frac{u_B}{u_{TP}}$ $\qquad$ $P = \frac{\mu u_{TP}}{d}.P^*$

Re is Reynolds number $\qquad$ Pe is Peclet number

E

1D Electrochemical Model

Case setup The domain, as shown in Figure E.1, is divided into 2 regions: slug region on either side of the bubble (1) and a film region (2). In the slug region, as discussed in section 5.1, the liquid circulates and is dominated by convection. A uniform concentration of $\bar{C}$ is assumed in the slug region. Depending on the reaction rate and velocity of slug, a small diffusion-layer appears close to the cathode, in which the concentration gradients are significantly high. It is assumed that diffusion layer thickness is the same as film thickness above the bubble. As mentioned in section 5.1, this assumption is not valid. But from a modelling perspective, it is still interesting to know what range of flow conditions make the assumption valid. Therefore, the diffusion layer close to the cathode with a thickness of δ is selected as the domain for the 1D model. At the interface, the concentration of CO_2 in water ($C^0_{CO_2}$) depends on the equilibrium between the gas phase & liquid phase and is assumed to be constant.

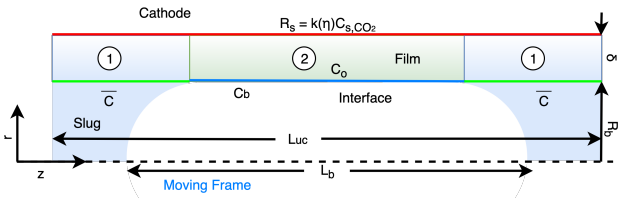

Figure E.1: Schematic representation of the domain for 1D Electrochemical model

Modelling Naturally, in the diffusion layer, only the diffusion is significant, and thus only diffusion terms are considered in the species transport equation, and the equation simplifies to Equation E.1.

$$\frac{\partial c}{\partial t} = D\left(\frac{\partial^2 c}{\partial z^2} + \frac{1}{r}\frac{\partial}{\partial r}r\frac{\partial c}{\partial r}\right) \tag{E.1}$$

Since the film thickness(δ) is much smaller compared to the unit cell length(L_{uc}), the concentration gradient in the z-direction is assumed minimal. Subsequently, the second derivative of the gradient, i.e. the diffusion term in the z-direction is considered insignificant. Equation E.1 can be simplified to a 1D problem and is written as Equation E.2 for steady-state.

$$\frac{\partial^2 c}{\partial \chi^2} \approx 0 \tag{E.2}$$

where χ is the radius in the new coordinate system, defined such that $\chi = r - R_b$. The boundary conditions are:

$$c(0,z) = \begin{Bmatrix} \bar{C}(t) & \forall \quad z \in \text{Slug region} \\ C^o_{CO_2} & \forall \quad z \in \text{Film region} \end{Bmatrix} \tag{E.3}$$

$$-D\frac{\partial c}{\partial \chi}|_{\delta,z} = k(\eta).c(\delta,z) \tag{E.4}$$

where $k(\eta)$ is first order rate constant given by Equation 3.11, as a function of overpotential (η). The solution to Equation E.2 is given by:

$$c(\chi,z) = c(0,z)\left(1 - \frac{Da(\eta)}{1+Da(\eta)}.\frac{\chi}{\delta}\right) \tag{E.5}$$

where, $Da(\eta) = \frac{k(\eta)\delta}{D}$ is Damkohler number. From Equation E.5, for small over-potentials i.e. for $Da(\eta) << 1$, $c(\chi,z) = c(0,z)$ giving an uniform concentration in the film showing that system is rate-limited and for large over potentials i.e for $Da(\eta) >> 1$, the wall concentration, $c(\delta,z) \to 0$, showing a mass transfer limited system. Notably, the average bulk concentration in slug region($\bar{C}$) changes as the reaction proceeds for long time. Also, during this period, the bubble starts shrinking. Therefore, a quasi-steady-state approach as explained in subsection 3.1.2 is also used for the 1D model.

The average bulk concentration can be determined by looking at the slug region as a CSTR with uniform concentration ($\bar{C}$) in the bulk region as shown in the Figure E.2.

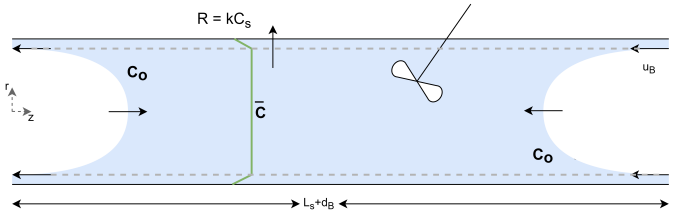

Figure E.2: Slug region of the Taylor flow

Mass balance over the bulk region of slug is given by:

Accumulation = In - Out + Generation

$$V_s \frac{\partial \bar{C}}{\partial t} = k_L.4\pi R_b^2.(C_O - \bar{C}) - 2\pi R_b(L_s + d_b).J|_{R_b} + 0 \tag{E.6}$$

where, $V_s \approx \pi R_b^2 L_s$, k_L is mass transfer coefficient at the bubble caps, $J|_{R_b}$ is the flux of CO_2 at radius R_b. From Equation E.5, the flux at R_b is given by $J|_{R_b} = \frac{D}{\delta}.\frac{Da(\eta)}{1+Da(\eta)}\bar{C}$. The expression for mass transfer coefficient is obtained from correlation derived from the penetration theory and stated as $k_L = 2\sqrt{\frac{2Du_B}{\pi^2 d}}$ [27, 31, 41]. Equation E.6 can be rewritten as:

$$\frac{\partial \bar{C}}{\partial t} = \frac{4k_L}{L_s}.(C_O - \bar{C}) - \frac{2D(1+\frac{d}{L_s})}{\delta R_b}.\frac{Da(\eta)}{1+Da(\eta)}.\bar{C} \tag{E.7}$$

At steady-state, the average concentration is given by Equation E.8.

$$\bar{C} = \frac{k_L C_{CO_2}^o}{k_L + k'} \tag{E.8}$$

where, $k' = \frac{D}{\delta} \times \frac{Da(\eta)}{1+Da(\eta)} \times \left(1 + \frac{L_S}{d_b}\right)$.

The total mass transfer rate at the cathode is determined using the equations for average concentration and concentration profile. Equation E.9 gives the total mass transfer rate at the cathode.

$$\nu_m^{wall} = \frac{D}{\delta}.\frac{Da(\eta)}{1+Da(\eta)}.(C_{CO_2}^o.A_f + \bar{C}A_s) \tag{E.9}$$

where A_f is the surface area of film region, A_s is the surface area of the slug region. The total current density (j) is calculated from mass transfer rate using Faraday's law and is given by Equation E.11

$$j = nF \times \frac{\nu_m^{wall}}{A_f + A_s} \tag{E.10}$$

$$j = \frac{nFD}{\delta}.\frac{Da(\eta)}{1+Da(\eta)}.\frac{C_{CO_2}^o.A_f + \bar{C}A_s}{A_f + A_s} \tag{E.11}$$

The limiting current density (j_{lim}) is calculated using Equation E.11 to give Equation E.12.

$$j_{lim} = \frac{nFD}{\delta}.\frac{C_{CO_2}^o.A_f + \bar{C}A_s}{A_f + A_s} \tag{E.12}$$

At steady-state, assuming net-flux through inlet and outlet is zero, the total number of moles of CO_2 getting consumed at the wall is equal to the total number of moles supplied at the interface. Mathematically, this is written as:

$$-C_b \frac{\partial V_b}{\partial t} = \nu_m^{wall} \tag{E.13}$$

F

Figures

In this chapter, enlarged of some small figures are shown.

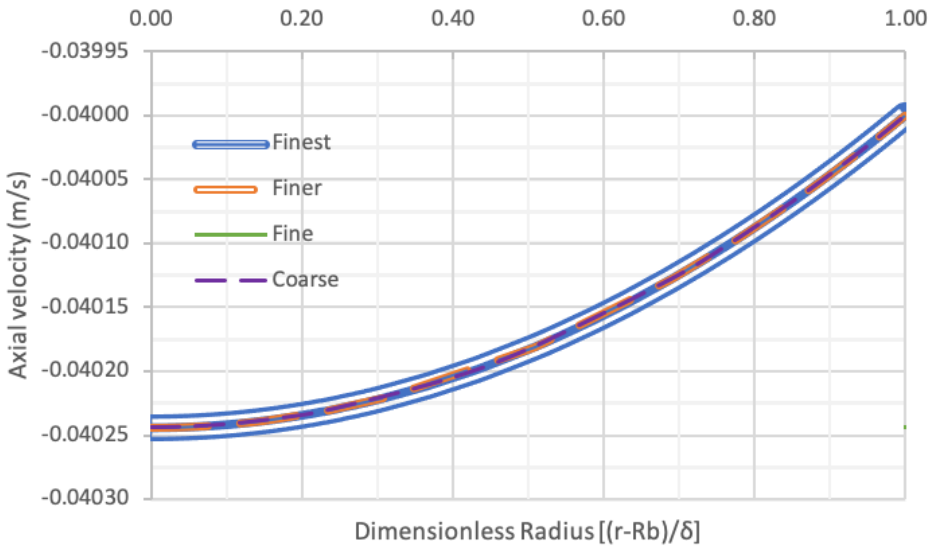

Velocity profiles in film for different meshes.

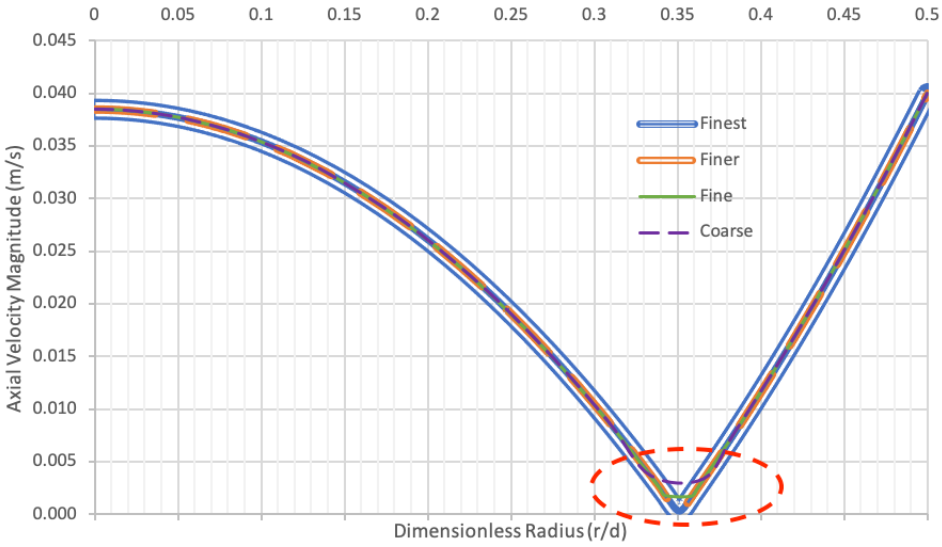

Velocity profiles in liquid slug for different meshes.

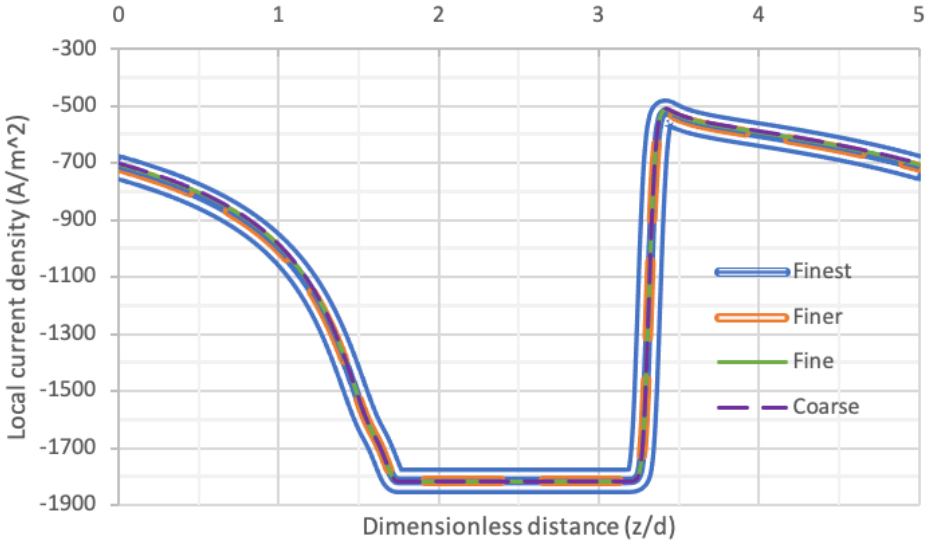

Local current density at cathode for different mesh sizes

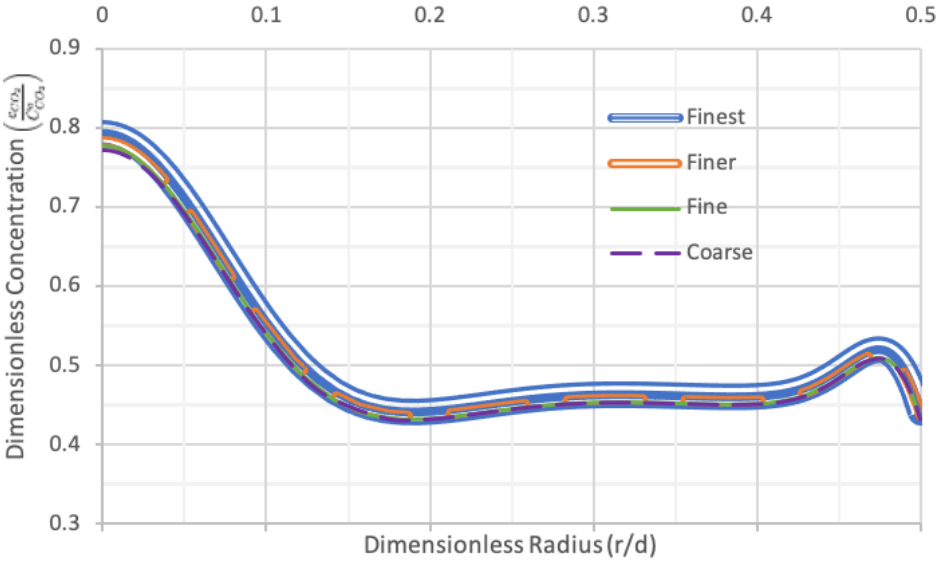

CO_2 concentration profile in liquid slug for different meshes